

1-1-2007

High Strain-Rate Finite Element Simulations

Jeremy Len Mowry

Follow this and additional works at: <https://scholarsjunction.msstate.edu/td>

Recommended Citation

Mowry, Jeremy Len, "High Strain-Rate Finite Element Simulations" (2007). *Theses and Dissertations*. 2493.

<https://scholarsjunction.msstate.edu/td/2493>

This Graduate Thesis - Open Access is brought to you for free and open access by the Theses and Dissertations at Scholars Junction. It has been accepted for inclusion in Theses and Dissertations by an authorized administrator of Scholars Junction. For more information, please contact scholcomm@msstate.libanswers.com.

HIGH STRAIN-RATE FINITE ELEMENT SIMULATIONS

By

Jeremy Len Mowry

A Thesis
Submitted to the Faculty of
Mississippi State University
in Partial Fulfillment of the Requirements
for the Degree of Master of Science
in Mechanical Engineering
in the Department of Mechanical Engineering

Mississippi State, Mississippi

August 2007

HIGH STRAIN-RATE FINITE ELEMENT SIMULATIONS

By

Jeremy Len Mowry

Approved:

Mark F. Horstemeyer
Center for Advanced Vehicular Systems
Chair in Computational Solid Mechanics
Professor of Mechanical Engineering
(Director of Thesis)

John T. Berry
E.P. Coleman Professor of
Mechanical Engineering
(Committee Member)

Steven R. Daniewicz
Professor of Mechanical Engineering
Graduate Coordinator of the Department
of Mechanical Engineering
(Committee Member)

Philip M. Gullett
Associate Professor of
Civil Engineering
(Committee Member)

W. Glenn Steele
Interim Dean of the James Worth
Bagley College of Engineering

Name: Jeremy Len Mowry

Date of Degree: August 11, 2007

Institution: Mississippi State University

Major Field: Mechanical Engineering

Major Professor: Dr. Mark F. Horstemeyer

Title of Study: HIGH STRAIN-RATE FINITE ELEMENT SIMULATIONS

Pages in Study: 84

Candidate for Degree of Master of Science

A hydrocode and an explicit finite element code were used to evaluate functionally graded material impacts, meteor impacts, and split Hopkinson pressure bar specimens. Modeling impacts of functionally graded projectiles revealed that density was the primary material characteristic controlling the shock wave profile. A parametric study of material order for functionally graded armor showed that arranging the weaker material in front created the greater stopping power. By modeling an array of meteor impact scenarios, deformation and stress were shown to occur at great depths and possibly cause tectonic movement, like subduction. Three proposed Hopkinson specimens, which were designed to produce either shear or tensile reactions under compressive loading, were evaluated. For two of these specimens, improved stress and strain equations were presented.

DEDICATION

I would like to dedicate this work, in memory, to my grandparents—James and Letha Chain, and Virgil and Laura Mowry.

ACKNOWLEDGMENTS

I would like to thank those who have made this work possible. First, I would like my advisor, Dr. Mark Horstemeyer, for giving me this opportunity, input, and encouragement. Second, I would like to thank Dr. John Berry for his encouragement and influence on my academics and career. Third, I would like to thank Dr. Steven Daniewicz and Dr. Philip Gullett for their input and approval of this thesis. I would also like to thank Dr. Corbett Battaile, Matthew Tucker, Kiran Solanki, and David Oglesby for their mentoring and/or influences on this research. Beyond the aforementioned names, I would like to thank the staff at the Center for Advanced Vehicular Systems for their time, space, financial support, and other resources. Finally, I would like to thank my Lord, my family, and my friends for their unwavering support.

TABLE OF CONTENTS

| | Page |
|--|------|
| DEDICATION | ii |
| ACKNOWLEDGMENTS | iii |
| LIST OF TABLES | vi |
| LIST OF FIGURES | vii |
| CHAPTER | |
| 1. INTRODUCTION | 1 |
| Dynamic Material Response..... | 1 |
| Stress Waves..... | 1 |
| Shock Waves | 4 |
| Computational Solutions | 6 |
| Applications..... | 7 |
| REFERENCES | 9 |
| 2. EVALUATION OF FUNCTIONALLY GRADED MATERIALS DURING FLIER PLATE IMPACT TESTING..... | 10 |
| Introduction | 10 |
| Flier Plate Impact Testing | 10 |
| Functionally Graded Materials | 11 |
| Functionally Graded Projectile Modeling | 13 |
| Functionally Graded Projectile Results..... | 16 |
| Functionally Graded Armor Modeling..... | 21 |
| Functionally Graded Armor Results | 22 |
| Functionally Graded Material Conclusions..... | 22 |
| REFERENCES | 24 |

| CHAPTER | Page |
|--|------|
| 3. EVALUATION OF STRESS WAVES CREATED BY A METEOR STRIKING THE EARTH | 25 |
| Introduction | 25 |
| Modeling Impacts with Earth – A Background | 25 |
| Crustal Effects of Impacts with Earth | 27 |
| Modeling Meteor Impacts | 28 |
| Meteor Impact Results | 35 |
| Meteor Impact Conclusions | 48 |
| REFERENCES | 50 |
| 4. VALIDATION OF TENSION AND SHEAR SPECIMENS UNDER DYNAMIC COMPRESSIVE LOADING | 52 |
| Introduction | 52 |
| Proposed Hopkinson Techniques | 53 |
| Finite Element Validation | 59 |
| M-Shaped Specimen | 60 |
| Shear-Compression Specimen | 65 |
| Hat-Shaped Specimen | 69 |
| Dynamic Stress States | 73 |
| Specimen Conclusions | 74 |
| REFERENCES | 75 |
| 5. CONCLUSIONS | 77 |
| APPENDIX | |
| A. METEOR IMPACT MATERIALS | 79 |
| B. DYNAMIC SPECIMEN MATERIAL MODEL | 83 |

LIST OF TABLES

| TABLE | Page |
|-------|--|
| 2.1 | Material models used in flier plate simulations 16 |
| 2.2 | Projectile velocity at 2 microseconds after impact with FG plate. The stopping power is dependent on the ordering and grading thickness.....22 |
| 3.1 | Meteor simulation array 31 |
| 3.2 | Comparison of tracer displacements for rectangular and circular meshing schemes with different meteor sizes. The tracer was initially at (3km, -110km). 34 |
| 3.3 | Two-dimensional meteor radius conversion to three-dimensional..... 35 |
| 3.4 | Cell length comparison using tracer displacement [initially at (10km, -550km)] 35 |
| A.1 | Material models for meteor simulations..... 81 |
| A.2 | BCJ models for wet and dry olivine at high temperatures 82 |
| B.1 | Bammann plasticity property values and constants for Al 6061-T6 [Guo et al., 2005] 84 |

LIST OF FIGURES

| FIGURE | Page |
|---|------|
| 1.1 Stress-strain curve under uniaxial strain illustrating the slope, $\Delta\sigma/\Delta\varepsilon$, for several stress levels [Nicholas and Recht, 1990]..... | 3 |
| 1.2 Strain profile for an elastic-plastic stress wave illustrating the leading elastic front and the slower plastic waves [Nicholas and Recht, 1990] | 4 |
| 1.3 Shock wave variables of interest determined by governing equations | 6 |
| 2.1 Flier plate impact test arrangement using air pressure as propulsion | 11 |
| 2.2 Uniaxial stress recorded in a copper target sample created during the impact of (a) copper, (b) functionally graded aluminum-to-copper, and (c) composite aluminum-copper flat specimens. This figure illustrates the effect of projectile composition on the induced stress..... | 12 |
| 2.3 Flier plate simulation arrangement (mirrored about the y-axis)..... | 14 |
| 2.4 Volume fraction of each metal by cell location throughout the two-millimeter graded layer. This finite scheme was used to simulate the linear transition from metal A to metal B. | 15 |
| 2.5 Functionally graded projectile simulation arrangement with tracer locations (dots) and the stress recorded by these tracers. The stress deviation, which occurred around 2.5 microseconds, indicated the end of the uniaxial stress state. | 17 |
| 2.6 Uniaxial stress for different forward metals (metal B) during the flier plate simulation. The backing metal (metal A) is copper. This figure illustrates how the initial stress magnitude differed with the leading metal. | 18 |
| 2.7 Uniaxial stress for different backing metals (metal A) during the flier plate simulation. The forward metal (metal B) is copper. This figure illustrates how the second stress event's magnitude differed with the backing metal. | 19 |

| | | |
|-----|--|----|
| 2.8 | Reflected shock wave's leading stress by location. Aluminum is the forward metal. This figure illustrates how the aluminum-to-copper graded layer reacts to a stress wave. | 20 |
| 2.9 | Reflected shock wave's leading stress by location. Copper is the forward metal. This figure illustrates how the copper-to-aluminum graded layer reacts to a stress wave. | 21 |
| 3.1 | Subduction of an oceanic plate beneath a continental plate [Kious and Tilling, 1996] | 28 |
| 3.2 | Meteor impact simulation geometry with material labels, temperature profile, and pressure profile | 29 |
| 3.3 | Two-dimensional meteor impact simulation for investigation of rectangular and circular meshing schemes | 34 |
| 3.4 | Pressure during the meteor impact simulation at 0, 5, 10, and 15 seconds after impact. This figure illustrates the stress wave decay as energy was absorbed by more of the Earth. | 36 |
| 3.5 | Initial and maximum pressure versus depth for the base meteor impact simulation. The pressure increase (difference between initial and maximum) illustrates pressure decay with depth. | 37 |
| 3.6 | Positive and negative shear stress during the meteor impact simulation at 25, 50, and 85 seconds after impact. This figure illustrates the shear stress just behind the pressure wave (time = 25s), sustained uniform shear (time = 50s), and reversed shear caused by upward moving material (time = 85s). | 38 |
| 3.7 | Maximum pressure increase in the Earth's depths due to 5-km meteor impacts of 10, 40, and 70 km/s | 39 |
| 3.8 | Maximum pressure increase in the Earth's depths due to 40-km/s impacts of 9-, 7-, 5-, 3-, and 1-km meteors. The three-dimensional radii would be 21.8, 19.2, 16.2, 12.8, and 8.2 km. | 40 |
| 3.9 | Tracer paths during meteor impacts at angles of 90, 80, 45, and 25 degrees from horizontal. The thicker line indicates the meteor's flight path. These tracers, originating 5 km from the boundary, illustrate how the material flow is opposite of the impact direction. | 42 |

| | | |
|------|--|----|
| 3.10 | Tracer paths during meteor impacts at 0, 10, and 20 kilometers from the tectonic boundary. The thicker line indicates the meteor's flight path and impact location. These tracers, originating 5 km from the boundary, illustrate how the material at a boundary flowed by impact location. | 43 |
| 3.11 | Tracer paths during meteor impacts using (a) simple yield strengths and (b) BCJ plasticity models for olivine. The thicker line indicates the meteor's flight path and impact location. The tracers originate 5 km from the boundary. | 44 |
| 3.12 | Positive and negative shear stress during the meteor impact simulation at 25, 50, and 85 seconds after impact using the BCJ plasticity model for wet and dry olivine. These shear stresses are greater and more asymmetric than the base simulation..... | 45 |
| 3.13 | Plastic strain rate recorded at 60-km deep on each side of the tectonic boundary illustrating the similar strain rates in the base simulation..... | 47 |
| 3.14 | Plastic strain rate recorded at 60-km deep on each side of the tectonic boundary illustrating the slightly different strain rates in the BCJ-olivine simulation..... | 48 |
| 4.1 | M-shaped specimen geometry presented by Mohr and Gary [2007] which is intended to produce tension in the gage section when compressed. The large arrows indicate compressive loading..... | 55 |
| 4.2 | Shear-compression specimen presented by Rittel et al. [2002] where (a) is the side view and (b) is an angled view. This specimen is intended to produce shear in the gage section when compressed. The large arrows indicate compressive loading. | 57 |
| 4.3 | Hat-shaped specimen presented by Meyer and Kruger [2000]. This cross section is rotated about the cylindrical axis. This specimen is intended to produce shear in the gage section when compressed. The large arrows indicate compressive loading. | 59 |
| 4.4 | Deformation of the m-shaped specimen (time = 0.11 ms) (a) with friction applied at ends and (b) with the spacer block and base frame proposed by Mohr and Gary [2007]. Both simulations started with the same incident wall velocity..... | 61 |
| 4.5 | Uniaxial stress distribution in the m-shaped specimen's gage section taken from the finite element simulation. The front edge is the free edge, and the opposite edge is the symmetry border..... | 62 |

| | | |
|------|--|----|
| 4.6 | Finite element uniaxial stress-strain results for the m-shaped specimen (~600/s) from (a) the gage section and (b) calculations using end force and displacements [Mohr and Gary, 2007]. The (a) curve is the uniaxial stress-strain relationship in the gage section, and the (b) curve is the approximate which would be calculated from experimental data. The strain history from (b) was used to deform a single element under (c) plane strain conditions and (d) free conditions. The stress-strain curve (e) for a simple tension experiment (622/s) [Johnson and Holmquist, 1989] has a much lower stress than the m-shaped results. | 64 |
| 4.7 | Finite element uniaxial stress-strain results for the m-shaped specimen (~1500/s) from (a) the gage section and (b) calculations using end force and displacements [Mohr and Gary, 2007]. The higher rate produced more fluctuation in the results compared to Figure 4.6. | 65 |
| 4.8 | Plastic strain in the gage section of the Rittel et al. [2002] shear-compression specimen from the finite element simulation | 66 |
| 4.9 | Equivalent stress-plastic strain results (~1400/s) for the Rittel et al. [2002] shear-compression specimen (a) recorded in the gage section and (b) calculated from end force and displacements. These results are from the finite element simulation. | 67 |
| 4.10 | Shear stress-strain results (~2500/s) for the Rittel et al. [2002] shear-compression specimen (a) calculated from end force and displacements and (b) recorded in the gage section. These results are from the finite element simulation. | 68 |
| 4.11 | Stress contour plot of hat-shaped specimen cross section as calculated by the finite element simulation (time = 0.6 ms) | 70 |
| 4.12 | Shear stress-strain results (~750/s) for the hat-shaped specimen (a) recorded in the gage section, (b) calculated from end force, end displacements, and specimen stiffness, (c) calculated assuming all displacement occurs in the gage section. These results are from the finite element calculation. | 72 |
| 4.13 | Shear stress-strain results (~2500/s) recorded in the gage sections of the hat-shaped specimen and the shear-compression specimen simulations illustrating the difference in stress states between these two specimens. Dynamic torsion experiments (232/s) yield slightly lower stress values..... | 73 |

| | | |
|------|---|----|
| 4.14 | Single element simulation stress-strain curves illustrating the material reaction to different stress states. Each case was given the same strain history (~575/s) and material (Al 6061-T6). | 74 |
| A.1 | Material diagram for meteor simulations | 80 |

CHAPTER 1

INTRODUCTION

Dynamic Material Response

The study of dynamic material response is becoming more important as it is being considered in design. Whether it is a baseball bat impacting a ball, a bullet impacting armor, or an explosion creating a desired deformation, the designer utilizes the knowledge of dynamic material behavior to create the desired effect. However, this area of material science has not received the attention given to quasi-static material response; this is most likely due to the complexity of dynamic behavior and the fact that one must first understand the quasi-static nature of materials. The main difference that distinguishes dynamic loading from quasi-static loading is the lack of static equilibrium in the material. For the quasi-static case, the material stress state is at or near equilibrium throughout the loading history. On the contrary, dynamic loading is characterized by inertia effects, stress lacking the time to reach equilibrium, and the resulting stress waves. This flow of stress and the subsequent material deformation must be understood to design for dynamic response.

Stress Waves

Understanding stress waves is the key element to understanding dynamic material response and begins with understanding stress waves during uniaxial strain. For the

simplest case, a small impact produces an elastic wave which travels at the medium's wave speed given by the following equation:

$$c = \sqrt{\frac{E}{\rho}} \quad (1-1)$$

where E is the medium's elastic modulus and ρ is the medium's density [Meyers, 1994].

The wave profile becomes more complicated when the stress wave is greater than the material's yield strength. Yielding, in dynamic studies, is normally quantified by the stress in the uniaxial strain direction during yielding; this stress is referred to as the Hugoniot elastic limit (HEL). The largest elastic stress wave magnitude is the HEL. Stress beyond the HEL travels at a speed based on the instantaneous slope of the stress-strain curve as shown by the following equation:

$$v_p = \sqrt{\frac{\frac{d\sigma}{d\varepsilon}}{\rho}} \quad (1-2)$$

where σ is the stress and ε is the strain [Meyers, 1994]. The plastic region of a uniaxial-strain stress-strain curve is concave up as shown by Figure 1.1; therefore, as stress is increased, the plastic wave speed is also increased. Since the larger plastic waves travel faster than weaker plastic wave, the weaker waves are overtaken, and the plastic wave velocity becomes an average velocity. For example, the slope of AB in Figure 1.1 would be used to determine the plastic wave speed for a stress wave equal to the stress at B. Figure 1.2 illustrates the typical elastic-plastic wave profile. For higher stresses, the plastic stress-strain slope (AC in Figure 1.1) will equal the elastic modulus so that all the

elastic and plastic portions of the stress wave have the same velocity. For stresses above this, the plastic wave velocity will be greater than the elastic wave velocity. When the elastic wave is overtaken, the entire stress front travels at a speed based on the average stress-strain slope (OD in Figure 1.1). This single stress wave is called a shock wave.

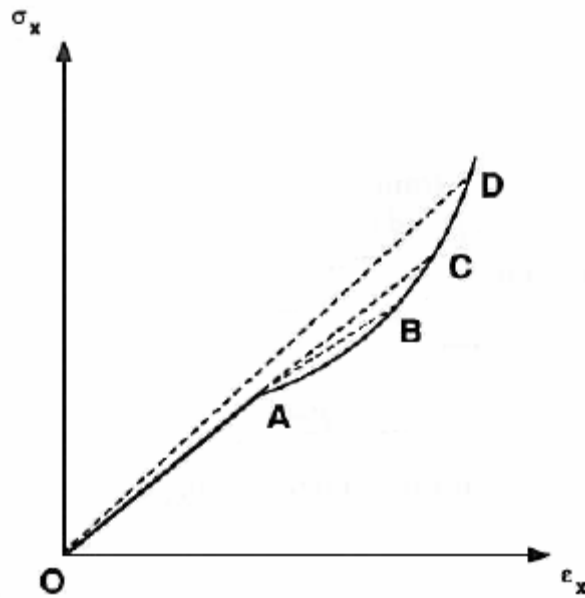


Figure 1.1 Stress-strain curve under uniaxial strain illustrating the slope, $\Delta\sigma/\Delta\epsilon$, for several stress levels [Nicholas and Recht, 1990]

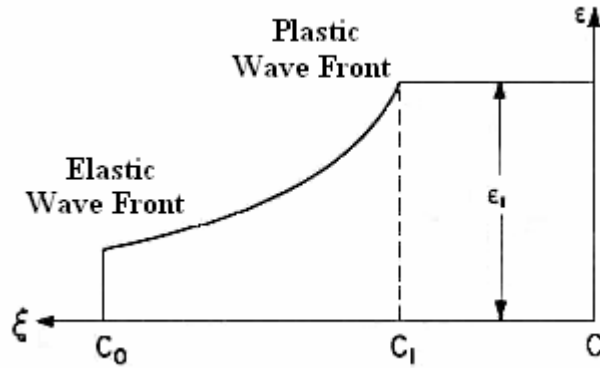


Figure 1.2 Strain profile for an elastic-plastic stress wave illustrating the leading elastic front and the slower plastic waves [Nicholas and Recht, 1990]

Shock Waves

The material response to shock wave loading is determined by several governing equations. Conservation of mass, momentum, and energy applied at the shock wave front are used to determine the relationship among the density, material velocity (u), stress, internal energy, and the shock wave velocity (U) (see Figure 1.3). Since these five variables exist in the three conservation equations, two variables remain independent. A fourth relationship is established through experimental work. By holding three of the variables constant and varying another, the response in the fifth variable is obtained and plotted as the Hugoniot curve. The simplest Hugoniot curve is found by recording material velocity, u , and shock wave velocity, U . This u - U relationship is modeled by a polynomial equation, and for many materials, this curve may be represented by the following linear equation:

$$U = c + S \cdot u \quad (1-3)$$

where c is the elastic wave speed and S is some material-dependent constant [Nicholas and Recht, 1990]. The most common Hugoniot curve is the pressure-specific volume (P-V) curve. With this curve and the three conservation equations, one variable must be known to solve the governing equations. Since the Hugoniot curves are found for only certain conditions, the curves must be adjusted to be applicable for other conditions. The most common form of adjustment is referred to as the equation of state (EOS). A typical equation of state relates pressure, volume (or density), and internal energy using the assumption of hydrostatic compression; so this equation of state gives pressure as a function of volume and internal energy. For solving problems with large amounts of energy, this relationship is crucial to obtaining acceptable results. Equation of state may be tabulated (SESAME) or calculated [Pierazzo and Collins, 2003; Nicholas and Rajendran, 1990]. A common calculated EOS is the Mie-Grüneisen approximation. The Mie-Grüneisen EOS relates pressure, volume, and internal energy as follows:

$$P - P_H = \frac{\gamma}{V} \cdot (E - E_H) \quad (1-4)$$

where P is pressure, V is volume, E is internal energy, γ is the Grüneisen parameter, the subscript H denotes the reference Hugoniot curve [Meyers, 1994]. The Grüneisen parameter is material dependent and has been experimentally obtained for many materials. These governing equations along with Newton's laws of motion are applied to complex problems using discrete computational methods [Collins, 2002].

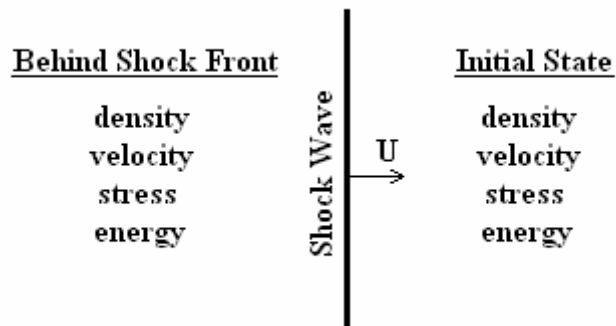


Figure 1.3 Shock wave variables of interest determined by governing equations

Computational Solutions

Eulerian and Lagrangian computational codes have been adapted or created to handle stress wave propagation. In Eulerian codes, the material moves through the computational cells. In Lagrangian finite element codes, the computation elements form the component, and the elements move with the material. Explicit Lagrangian finite element codes were designed to calculate dynamic material response, and some (LS-DYNA, for example) are capable of using an EOS model to calculate shocked material response. However, these codes sometimes experience inaccuracy and failure to compute with large deformations [Zukas, 1990]. The results and computational timesteps in explicit finite element simulations are dependent upon the element lengths. A heavily distorted element is prone to inaccurate results and may even turn inside-out, ending all calculations. Some explicit finite element codes include element rezoning and element eroding algorithms to remove heavily distorted elements. However, rezoning and eroding can lead to inaccuracy. Explicit finite element modeling is most useful for mid-range velocities or medium deformation and is well adapted for modeling surface interaction.

The Eulerian finite difference codes, hydrocodes, have been developed to model shock wave propagation and treat material response as fluid flow [Collins, 2002]. Hydrocodes (CTH, for example) use constitutive models, conservation equations, and equations of state from the Eulerian view so that large deformations can be calculated. During large deformation, hydrocodes remain more stable than explicit finite element codes since the cells (Eulerian equivalent of an element) retain their shape from one timestep to the next. Since material is moved through the cells in hydrocodes, the surface interfaces are prone to diffusion in most of these codes. However, CTH and some other well-developed hydrocodes use an advanced scheme for the advection of material interfaces [Zukas, 1990]. Both of these code types, hydrocodes and explicit finite element codes, are useful in modeling dynamic material response, and the user must remember when each type is applicable.

Applications

The following chapters present the application of hydrocodes and explicit finite element codes to investigate several dynamic material responses. First, functionally graded materials were modeled as projectiles and as armor to determine the resultant shock wave profile and stopping power, respectively. By modeling with several material combinations, the material property controlling shock wave magnitude was determined. Second, the impact of a meteor with the Earth was modeled to determine the crust's response to such loading. Last, several split Hopkinson pressure bar specimen types were modeled to determine their validity. For two of the specimens, calculations were

presented to improve the experimentally calculated results. In all of these studies, accurate material modeling is the key to determining the dynamic material response.

REFERENCES

- Collins, G.S., "An Introduction to Hydrocode Modeling," University of Arizona, Department of Planetary Sciences, unpublished lecture notes, 1-16, 2002.
- Meyers, M.A., *Dynamic Behavior of Materials*, New York: John Wiley and Sons, Inc., 1994.
- Nicholas, T. and Rajendran, A.M., "Material Characterization at High Strain Rates," *High Velocity Impact Dynamics* (edited by Zukas, J.A.), New York: John Wiley and Sons, Inc., 127-296, 1990.
- Nicholas, T. and Recht, R.F., "Introduction to Impact Phenomena," *High Velocity Impact Dynamics* (edited by Zukas, J.A.), New York: John Wiley and Sons, Inc., 1-64, 1990.
- Pierazzo, E. and Collins, G., "A Brief Introduction to Hydrocode Modeling of Impact Cratering" in "Cratering in Marine Environments and on Ice," *Impact Studies* (edited by Henning, D., Burchell, M., and Claeys, P.), New York: Springer, 2003.
- Zukas, J.A., "Survey of Computer Codes for Impact Simulation," *High Velocity Impact Dynamics* (edited by Zukas, J.A.), New York: John Wiley and Sons, Inc., 593-714, 1990.

CHAPTER 2
EVALUATION OF FUNCTIONALLY GRADED MATERIALS
DURING FLIER PLATE IMPACT TESTING

Introduction

As functionally graded materials have become more common and better production methods have been created, their properties in impact dynamics have led to new designs in armor and projectiles. To test these designs, the flier plate experiment is typically utilized. This chapter identifies the material and geometrical properties which give functionally graded armor and projectiles their characteristics. This investigation utilized hydrodynamic simulations which were comparable to flier plate experiments. The functionally graded material was used as the projectile to determine the stress wave produced by different material combinations and was used as the target to determine the stopping ability due to material ordering and grading thickness.

Flier Plate Impact Testing

The flier plate experiment was designed to isolate a one-dimensional pressure wave measurement upon impact. For this experiment, a flat sample is launched at a flat stationary sample as shown in Figure 2.1. High velocities are used to create strain rates greater than 10000/s. All data is derived from the recorded particle velocities in the stationary target sample and the projectile velocity at impact. In many cases, the

relationship between the particle velocity and stress is known for the target sample; this relationship is the Hugoniot curve used. This experiment is typically used to determine high strain rate yield strength, spall strength, shock wave response, and equation of state data during uniaxial strain. Once the created pressure wave reflects against the specimen's sides, the deformation is no longer uniaxial. In a typical flier plate experiment, the uniaxial strain condition only exists for 5 to 40 microseconds after impact. [Nemat-Nasser, 2000]

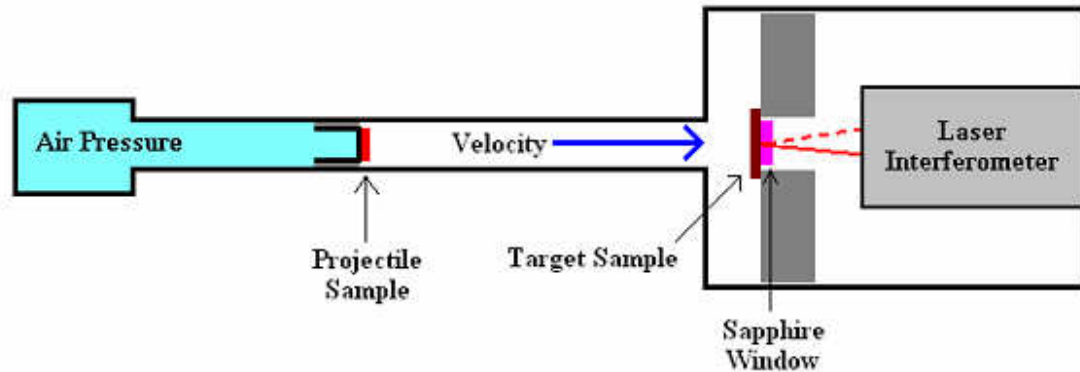


Figure 2.1 Flier plate impact test arrangement using air pressure as propulsion

Functionally Graded Materials

A functionally graded material (FGM) is a material which varies linearly (or semi-linearly) in some material property [Wang et al., 2002]; for a FGM which varies in volume fraction, as is the case of interest, one material fades from one hundred to zero percent volume fraction through the thickness while another material fades from zero to one hundred percent. For armor applications, a graded material is arranged to produce a less abrupt pressure wave allowing the material to absorb more energy as shown by

Kleponis et al. [2000] through CTH modeling; likewise, a graded projectile can produce a less abrupt pressure wave when compared to a solid material or a composite material as shown in Figure 2.2. Wang et al. [2002] stated that this less abrupt pressure wave allows more of the graded projectile's kinetic energy to convert to compressive energy in the target than an equivalent homogenous projectile. Using the flier plate experiment, which is designed to isolate the shock wave created by or induced in a material, the optimum FGM can be determined.

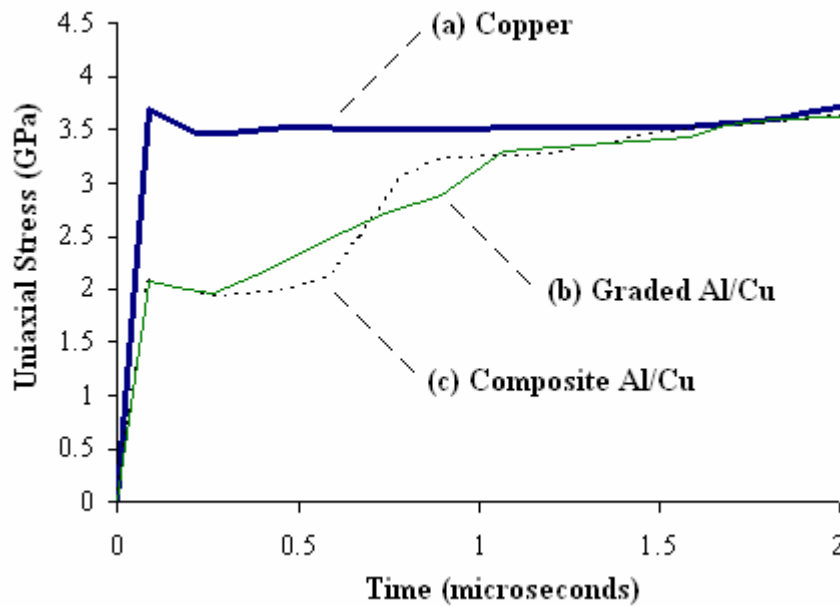


Figure 2.2 Uniaxial stress recorded in a copper target sample created during the impact of (a) copper, (b) functionally graded aluminum-to-copper, and (c) composite aluminum-copper flat specimens. This figure illustrates the effect of projectile composition on the induced stress.

For the experiment modeled here, the functionally graded material was used as the projectile, and the target was copper. The projectile was made by coating metal layers

on a copper cylindrical slug. The coating process began with a one-millimeter layer of metal A. Upon reaching one-millimeter, metal B was increasingly added so that the volume fraction faded linearly from metal A to metal B over a two-millimeter thickness. Then a one-millimeter metal B layer completed the 4-mm coating. This coating process created a slightly porous product. This method was used to create a variety of metal combinations.

Through finite element modeling of this flier plate experiment, the resulting shock waves could be modeled for a multitude of material combinations. By comparing these shock wave profiles, the material property dependence and ordering dependence of these functionally graded projectiles could be shown. As well, the use of functionally graded armor could be shown by the shock wave reflected into the graded projectile and by additional simulations in which the FGM was the target material. The importance of order and grading thickness would be revealed by these graded armor simulations.

Functionally Graded Projectile Modeling

CTH [McGlaun, 1990], a Lagrangian/Eulerian finite element code designed to calculate shock wave propagation, was used to simulate the reactions of the flier plate impact experiment. In this code, the geometry, material strengths, equations of state, constraints, interactions, and velocities were defined, and the reactions were calculated until they were no longer uniaxial. Upon building the geometric model, the material models could be easily changed so that many combinations could be studied. The materials of interest were copper, aluminum, low alloy steel, tool steel, titanium, tungsten, and iron.

This experiment could be modeled with only the projectile, copper target, sapphire backing, and aluminum mounting because no other components affect the results. The projectile, copper target, and sapphire backing were all cylindrical and share the same axis; for this reason, a two-dimensional cylindrical meshing was chosen. The model geometry is shown in Figure 2.3; this plot is a mirrored image (about the y axis). The dark material was an aluminum alloy used to hold the projectile and to support the target. The projectile was given an initial velocity of 200 m/s in the positive y direction. All material along the y axis was constrained in the x direction; also, the target-mounting aluminum was constrained against the top corner.

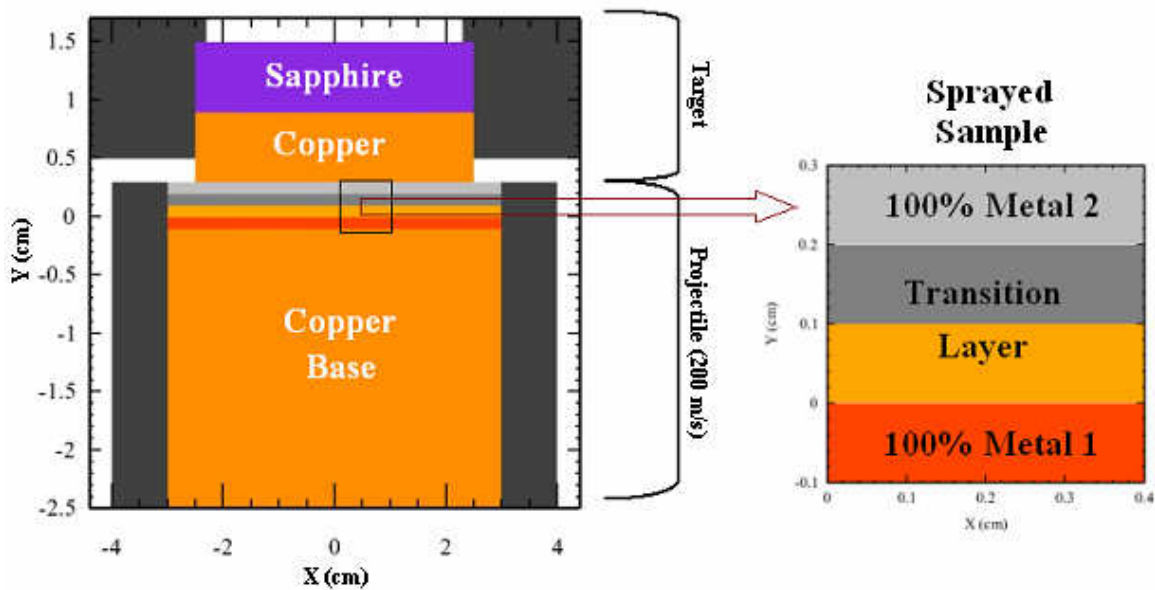


Figure 2.3 Flier plate simulation arrangement (mirrored about the y-axis)

The graded material layer was modeled using a finite approach; each computational cell layer through the thickness was given differing material volume

fractions. In the CTH model, the metal A/metal B transition occurs over ten cells (0.2 mm cell size, 2 mm graded thickness) as shown in Figure 2.4. This finite scheme is valid because CTH defines the material properties in a mixed material cell as the sum of the volume-fraction weighted material properties of the individual materials.

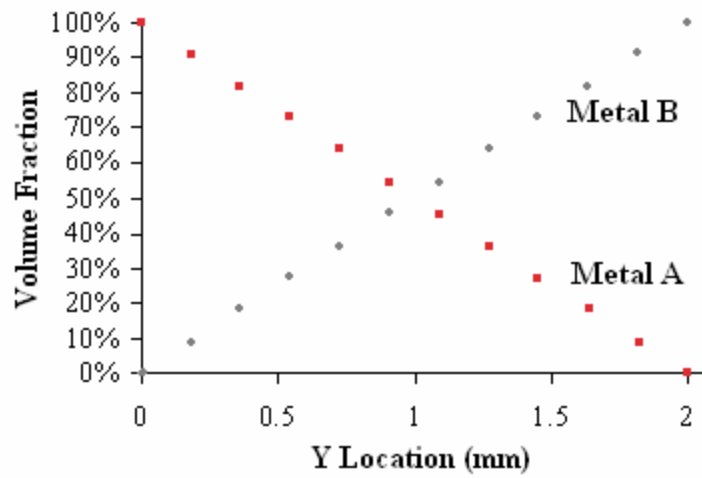


Figure 2.4 Volume fraction of each metal by cell location throughout the two-millimeter graded layer. This finite scheme was used to simulate the linear transition from metal A to metal B.

For each material in this simulation, a strength, fracture, and equation of state model was defined. The tensile strength and fracture strength for all metal components were governed by the Johnson-Cook viscoplastic model and the Johnson-Cook fracture model respectively. The sapphire's strength was controlled the von Mises criterion, and its fracture was controlled by simple fracture. The equation of state for all materials was calculated using the Mie-Grüneisen analytical formula. For the sprayed materials, the density used was ninety percent of their normal density; this density reduction is

representative of the density difference caused by the coating process. Table 2.1 summarizes the material models used for the simulations.

Table 2.1 Material models used in flier plate simulations

| Material | Strength Model | Fracture Model | Equation of State Model |
|-------------------|--------------------|--------------------|------------------------------|
| Mounting Aluminum | Al 2024 (JC) | Al 2024 (JC) | 1100 Al (Mgrun) |
| Target Copper | OFHC Copper (JC) | OFHC Copper (JC) | Copper (Mgrun) |
| Sapphire | Sapphire (Mises) | Sapphire (simple) | Sapphire (Mgrun) |
| Aluminum | 1100 Al (JC) | 1100 Al (JC) | 1100 Al (Mgrun) |
| Copper | OFHC Copper (JC) | OFHC Copper (JC) | Copper (Mgrun) |
| Iron | Iron (JC) | Iron (JC) | Iron - Epsilon Phase (Mgrun) |
| Low Alloy Steel | 1006 Steel (JC) | 1006 Steel (JC) | 304 Stainless Steel (Mgrun) |
| Titanium | Titanium (JC) | Titanium (JC) | Titanium (Mgrun) |
| Tool Steel | S7 Tool Steel (JC) | S7 Tool Steel (JC) | 304 Stainless Steel (Mgrun) |
| Tungsten | Tungsten (JC) | Tungsten (JC) | Tungsten (Mgrun) |

JC - Johnson Cook

Mises - Mises-Maxwell Criterion

Mgrun - Mie-Grüneisen

Functionally Graded Projectile Results

The shock wave profile for each simulation was recorded by specified tracers. A row of tracers was placed along the projectile/target boundary so that the reactions at the point of impact could be studied. This row of tracers differed in reactions when the shock wave travelled in more than one dimension as shown in Figure 2.5. The Y-Y stress plotted versus time for the tracers revealed the shock wave profile. The stress differed at 2.5 microseconds; so all reactions before this time were uniaxial. The shock wave profiles for all the metal combinations began with an abrupt initial stress (2.1 GPa in Figure 2.5) followed by a second stress event. These two stress wave features were controlled by the graded material layers.

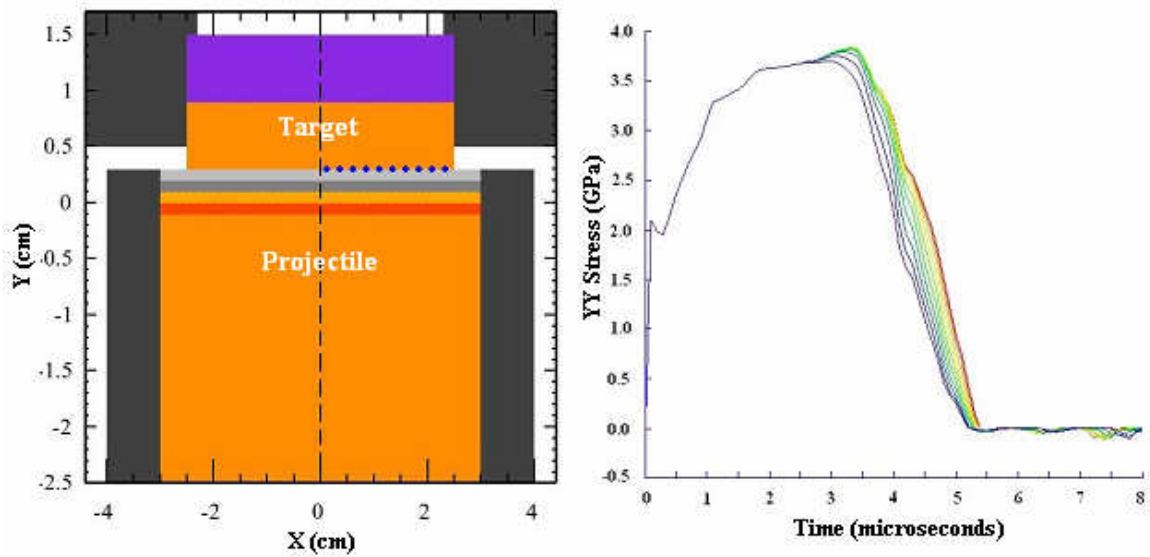


Figure 2.5 Functionally graded projectile simulation arrangement with tracer locations (dots) and the stress recorded by these tracers. The stress deviation, which occurred around 2.5 microseconds, indicated the end of the uniaxial stress state.

By holding the backing metal (metal A) constant, the forward metal's (metal B) effect on the initial stress was found to be mainly dependent on the density. The initial stress was solely dependent on the forward material for any metal combinations as shown in Figure 2.6. Increasing density increased this initial impact stress; this positive correlation was found with over 99.5% confidence. However, for copper, iron, low alloy steel, and tool steel, the densities were fairly close, and their initial stresses did not follow the density trend. The yield strength (or impedance) was found to be this secondary controlling material property. A larger impedance created a larger initial stress. This secondary controlling property becomes less effective as the impact speed is increased. In simulations ran at 10000 meters per second, the initial stresses are almost completely dependent on the density.

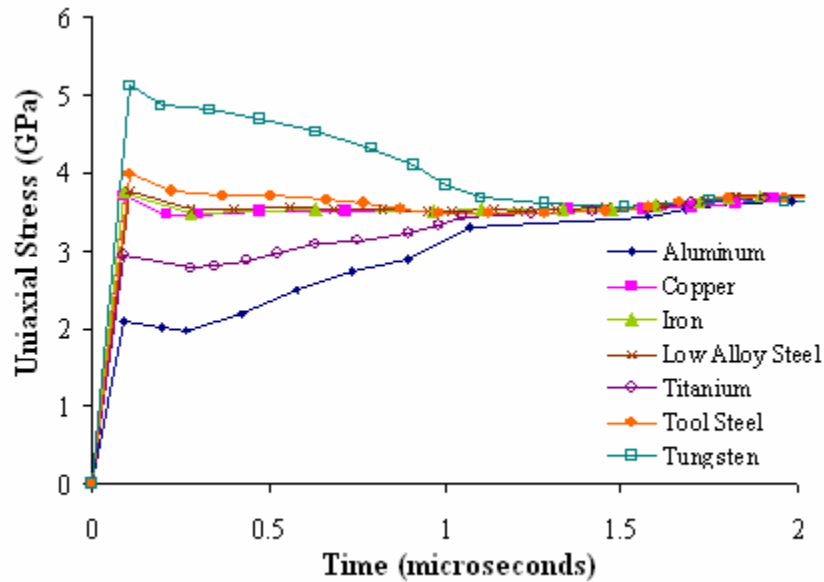


Figure 2.6 Uniaxial stress for different forward metals (metal B) during the flier plate simulation. The backing metal (metal A) is copper. This figure illustrates how the initial stress magnitude differed with the forward metal.

The second stress event was controlled by the backing metal (metal A). Following the initial stress, the stress wave magnitude would deviate based on the density of the backing metal relative to the density of the forward material. Again, positive correlation was found between density and stress with over 99.5% confidence. The secondary stress varied with backing metal, with aluminum causing the lowest dip in pressure and tungsten causing the highest peak in pressure (Figure 2.7). All of the metal combinations shared the same trend in secondary stress. As before, these pressure values were heavily dependent on density but differed somewhat for close densities. Again, impedance was found to be the secondary controlling property. The secondary stress magnitude was also influenced by the initial stress magnitude. Even with the same backing material, this secondary stress magnitude was dependent on the initial stress (Figure 2.6).

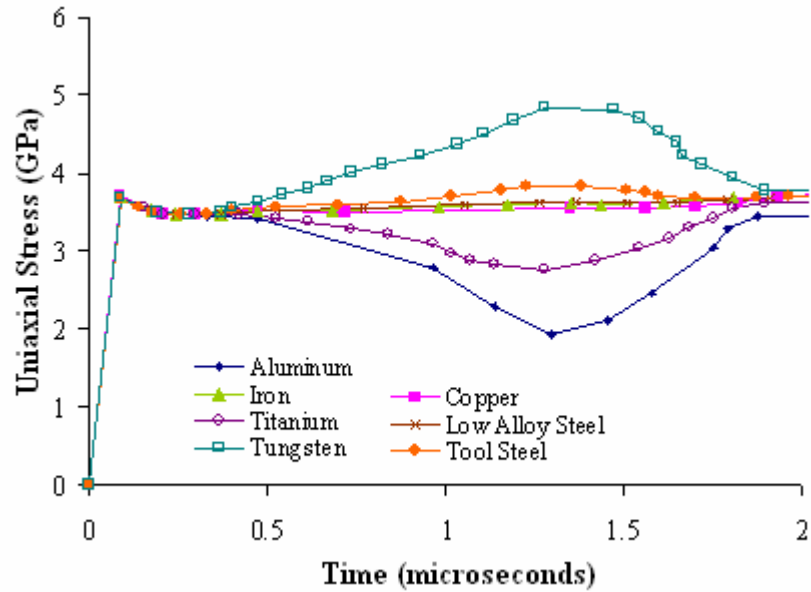


Figure 2.7 Uniaxial stress for different backing metals (metal A) during the flier plate simulation. The forward metal (metal B) is copper. This figure illustrates how the second stress event's magnitude differed with the backing metal.

To illustrate the use of functionally graded materials as armor, a column of tracers was placed through the functionally graded layer. These tracers record the leading edge magnitude of the reflected shock wave. The magnitude of the leading edge increased with acoustic impedance and could be estimated by the following formula derived by Bruck [2000] and adapted for this application:

$$f_T(z) = f_i \cdot \frac{\left(1 - \frac{Z(z)}{Z(0)}\right)}{\left(1 + \frac{Z(z)}{Z(0)}\right)} \tag{2-1}$$

where f_i is the initial stress magnitude, f_r is the stress magnitude at some location x in the graded layer, and Z is the acoustic impedance at x . As the acoustic impedance increased, the magnitude of the shock wave increased (Figure 2.8); likewise, decreasing the acoustic impedance decreased the shock wave magnitude (Figure 2.9).

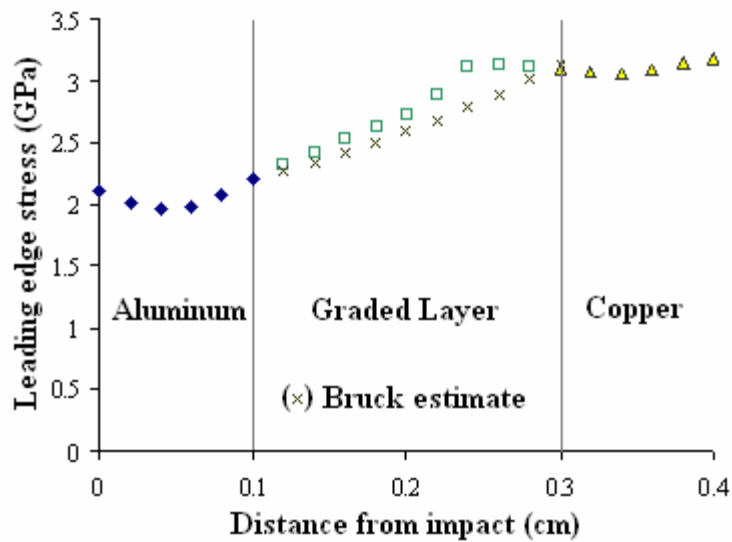


Figure 2.8 Reflected shock wave's leading stress by location. Aluminum is the forward metal. This figure illustrates how the aluminum-to-copper graded layer reacts to a stress wave.

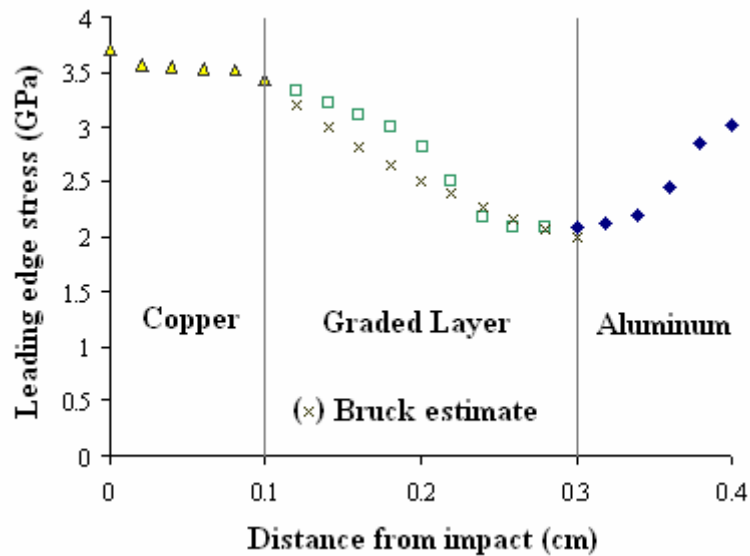


Figure 2.9 Reflected shock wave's leading stress by location. Copper is the forward metal. This figure illustrates how the copper-to-aluminum graded layer reacts to a stress wave.

Functionally Graded Armor Modeling

For this investigation of functionally graded material as armor, the modeling was much simpler. Using CTH, a four-millimeter target disc was arranged against a rigid boundary and was impacted by a solid tungsten rod at 200 meters per second. The target disc was composed of tungsten and aluminum as these were the extreme cases from the graded projectile study. With tungsten as the outermost metal and aluminum against the boundary, three simulations were analyzed using differing grading lengths (1.2 mm, 2.0 mm, 3.6 mm). Through these lengths, the metal transition occurred. These same graded layer lengths were used for simulations with the reverse ordering (aluminum as the outermost metal and tungsten against the boundary). As in the graded projectile study,

tracers were placed along the target-projectile interface to record stress, displacement, etc.

Functionally Graded Armor Results

For armor applications, the best material arrangement was the one which absorbs more of the projectile energy or has the greatest deceleration. Table 2.2 lists the projectile velocity at two microseconds for the six arrangements simulated. From the given velocities, aluminum as the outermost metal was the more efficient order for stopping the projectile; the weaker metal taking the initial impact was the more efficient method. Also, from these velocities, a thicker graded layer was shown to be more efficient at stopping the projectile.

Table 2.2 Projectile velocity at 2 microseconds after impact with FG plate. The stopping power is dependent on the ordering and grading thickness.

| Outer Metal | Bounded Metal | Grading Thickness (mm) | Projectile Velocity (m/s) |
|-------------|---------------|------------------------|---------------------------|
| Tungsten | Aluminum | 1.2 | 102.22 |
| Tungsten | Aluminum | 2.0 | 94.64 |
| Tungsten | Aluminum | 3.6 | 71.04 |
| Aluminum | Tungsten | 1.2 | 63.20 |
| Aluminum | Tungsten | 2.0 | 56.80 |
| Aluminum | Tungsten | 3.6 | 46.83 |

Functionally Graded Material Conclusions

For functionally graded projectiles, the initial stress magnitude upon impact was primarily dependent upon the forward material's density, and the second stress magnitude was primarily dependent upon the second material's density. After density, impedance was the controlling property. Knowing the trends for the two stress events, shock wave profiles can be designed to match the desired effect. For example, with the seven studied

materials, a tungsten-to-aluminum graded plate (aluminum being the forward material) would produce a shock wave with the greatest rise in stress between the initial and the secondary stress events. It follows that the reverse graded plate would create the largest drop in pressure. Also, because density is the main controlling factor, two materials with similar densities could be interchanged, giving the designer freedom to choose the metals by hardness, strength, ductility, etc.

For functionally graded armor applications, the ordering and transition length are vitally important to the projectile-stopping power. The weaker metal should be arranged as the outer layer, and the transition length should be as large as possible. The ordering and transition length conclusion was derived from simulations using two metals, but the same trend would follow in functionally graded materials with more than two metals.

REFERENCES

Bruck, H.A., "A One-Dimensional Model for Designing Functionally Graded Materials to Manage Stress Waves," *International Journal of Solids and Structures*, vol. 37, 6383-6395, 2000.

Kleponis, D.S., Mihalcin, A.L., and Filbey G.L., "Material Design Paradigms for Optimal Functional Gradient Armors," U.S. Army Research Laboratory, Aberdeen Proving Ground, MD, unpublished manuscript, 1-6, 2000.

McGlaun, J.M., Thompson, S.L., and Elrick, M.G., "CTH: A Three-Dimensional Shock Wave Physics Code," *International Journal of Impact Engineering*, vol. 10, 351-360, 1990.

Nemat-Nasser, S., "Introduction to High Strain Rate Testing," *ASM Handbook* (edited by Kuhn, H. and Medlin, D.), vol. 8, 427-461, ASM International, 2000.

Wang, C., Shen, Q., and Zhang, L., "A Flier-Plate Material with Graded Impedance Used in Dynamic High-Pressure Physics," *Journal of Wuhan University of Technology – Material Science Edition*, vol. 17, 4, 32-35, 2002.

CHAPTER 3
EVALUATION OF STRESS WAVES CREATED BY
A METEOR STRIKING THE EARTH

Introduction

This chapter presents the stress state and deformation in the Earth's depths during a sizable meteor impact. The pressure wave induced by a meteorite impact propagates deep into the Earth; if strong enough, this wave could cause failures, deformations, or material phase transitions detrimental to the stability of the crust. Eulerian hydrodynamic simulations were used to model an array of meteor impact scenarios and evaluate the stresses and deformation to a depth of 660 kilometers.

Modeling Impacts with Earth – A Background

Extraterrestrial bodies impacting the Earth has become a popular scientific topic since Alvarez et al. [1980] hypothesized a large impact causing the Cretaceous-Tertiary extinction and Hildebrand et al. [1991] proposed the Chicxulub crater as this impact's result. Other than this notable crater, over 150 impact features have been confirmed on the Earth, and many more are yet to be confirmed [Price, 2001]. Of these confirmed impact features, several are larger than the Chicxulub crater. These impacts have contributed to Earth's landscape just as impacts have contributed to the moon's

landscape. However, many of Earth's craters have been distorted or erased by erosion and tectonic motion.

Because planetary-scale experiments are not possible, most impact cratering studies focus on numerical modeling [Pierazzo and Collins, 2003]. When nuclear testing was in practice, geologists seized the opportunity to study crater formation even though explosive crater formation differed from impact crater formation. Progress in computational abilities has allowed for more understanding of impact cratering. O'Keefe and Ahrens [1977] and Ahrens and O'Keefe [1987] used finite-difference techniques to show the shock wave attenuation from meteorite impacts. Ahrens and O'Keefe [1987] also quantified energy loss to water and atmosphere (12 to 15% and 8%, respectively) before impacting rock; their ocean-impact model revealed the production of 4-km-tall tsunamis. Through observations and computational models like those of Ahrens and O'Keefe [1987], Melosh [1989] was able to divide impact crater formation into several stages. Pierazzo et al. [1998], Pierazzo and Melosh [1999], and Collins et al. [2002] have used numerical modeling, mainly hydrocodes, to simulate the Chicxulub impact event; their goals were to determine the meteor size and velocity as well as gas production during impact. Other scientists have used numerical modeling to show the impacts of very large bodies (100- to 2000-km radii) with the earth. Svetsov [2005] modeled asteroids (500 to 3000 km in diameter) impacting the Earth at 15 km/s to determine energy as a function of time and space from impact and to show the quantities of rock vapor produced. Teterov et al. [2004] showed the Earth's deformation by the impact of

large bodies (up to 2000-km radius) and crustal disruption created by smaller impactors (~160-km radius).

Crustal Effects of Impacts with Earth

Beyond cratering, impact effects, like those presented by Svetsov [2005] and Terev et al. [2004], have been presented in many ways. Price [2001] gave many examples of impact structures which are dated and located at the time and location of tectonic speed and/or direction shifts. In his book, Price [2001] listed fourteen instances of abrupt speed and/or direction shifts in tectonic tracks, and each of these shifts is associated with an impact event. Some geologists have suggested that large impacts could have instigated a worldwide flood by initiating tectonic subduction, which is shown in Figure 3.1. One such theory by worldwide flood researchers suggests that a bombardment of impacts would be sufficient to initiate subduction of tectonic plates. These impacts would have to create a 10^7 - to 10^8 -Pa pressure increase at a depth of 400 to 660 km below the Earth's surface. This pressure increase would be sufficient to cause two mineralogical solid state phase transitions, and these transitions to denser phases would initiate subduction. Another theory by worldwide flood researchers states that an impact could initiate subduction by creating a weakness (or weaknesses) in the Earth's crust; this weakness is formed by localization or concentrated deformation in narrow zones (shear bands). The weakening continues in these zones through the cycle of deformation, heating, and weakening. This strain rate difference between the subducting slab and the adjacent shear zone must be at least two orders of magnitude. The impact investigation,

described in this paper, focused on crustal stress and deformation to a 660-km depth and on possible localization.

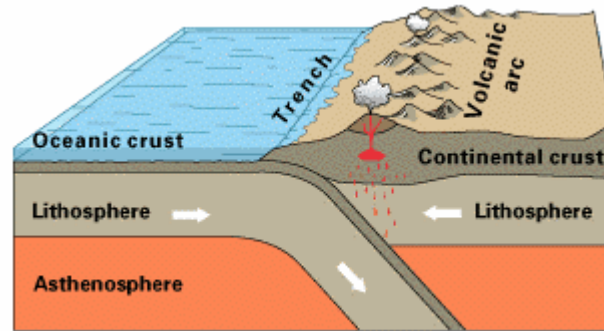


Figure 3.1 Subduction of an oceanic plate beneath a continental plate [Kious and Tilling, 1996]

Modeling Meteor Impacts

This investigation focused on crustal deformation; therefore the scale of this meteor impact simulation was created large enough to capture the effect on tectonic plates. In order to capture the possible subduction initiations, the model was constructed as the boundary of an oceanic tectonic plate and a continental tectonic plate; these simulations were completed using the Eulerian hydrocode CTH [Bell et al., 2003]. In several simulations, meteor impacts were modeled at and around the boundary. The initial geometry, materials, temperature, and pressure are shown in Figure 3.2. The modeled depth, 660 km, was chosen in order to capture the pressure increase needed for the mineralogical phase transition and because it is deeper than tectonic plates [Price, 2001]. The materials, temperature, and pressure which comprised the Earth were chosen based on the works by Wenk [2004]. Iron was chosen for the meteor's material because it is the densest material commonly found in meteors [Hutchison, 2004]; the high density

and strength of iron would cause the largest impact compared to other meteor materials. These simulations were calculated to 100 seconds after impact in order to capture the stress wave at the 660-km depth.

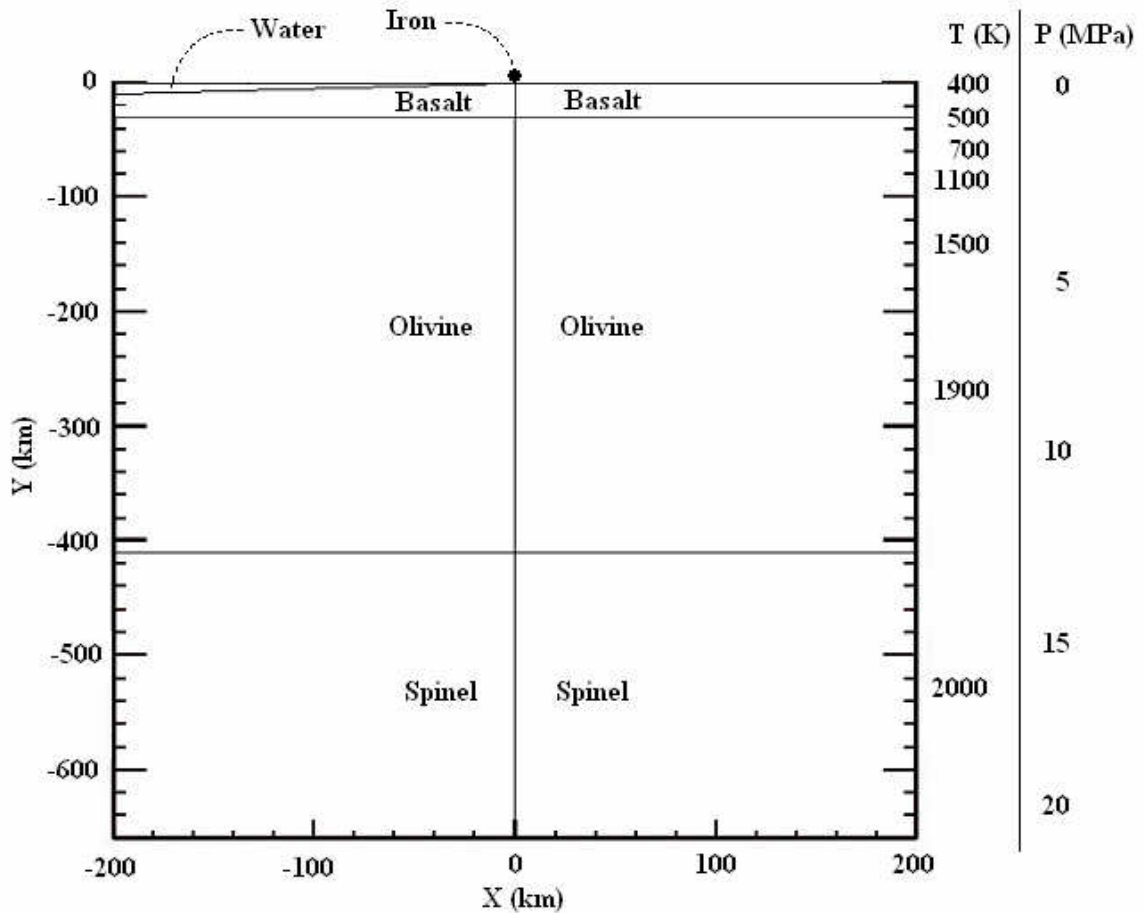


Figure 3.2 Meteor impact simulation geometry with material labels, temperature profile, and pressure profile

Each material was modeled using a plasticity model, an equation-of-state model, and a fracture model. Each material layer was subdivided into temperature layers so that the temperature-dependent behavior would be captured; these subdivisions and their

corresponding material numbers are displayed in Appendix A (Figure A.1). These material models are listed, in detail, in Appendix A (Table A.1). The meteor was represented using the Johnson-Cook plasticity model, a strain-rate and temperature dependent plasticity model [Bell et al., 2003]. All other materials' plasticity models were simple yield strengths. Some equation-of-state models already defined in CTH were used—iron, water, and basalt. The Mie-Grüneisen approximation was used to represent the equation of state for iron and water [Hertel and Kerley, 1998]; this approximation uses the Hugoniot as the reference and adjusts as relative density changes. The SESAME database method was used to represent the basalt's equation of state; this method interpolates data sorted by density and temperature. The equation-of-state models for olivine and spinel were created using constants listed by Ahrens and Johnson [1995] and using temperature-dependent constants listed by Anderson and Isaak [1995]. Anderson and Isaak [1995] listed the temperature-dependent constants for olivine and spinel up to 1500 K; higher temperature constants were extrapolated. (Note: The simulations were calculated using room temperature. All material models were adjusted so that, at room temperature, they performed as the temperatures listed in this work.)

The meteor sizes, speeds, and impact angles for this work were chosen to be similar to that of the Chicxulub impact. With typical impact speeds (20 to 40 km/s), the impactor must be at least 5 km in diameter to create the mineral phase-changing pressure wave. Ahrens and O'Keefe [1987] performed simulations for impactors traveling 5 to 45 km/s and suggested that the Chicxulub crater was formed by an asteroid approximately 10 km in diameter. Mason [1962] and Olivier [1925] listed maximum meteor impact

speeds of 70 and 75 km/s, respectively. As for impact angles, the most probable impact angle for a random impact would be 45 degrees from horizontal [Melosh, 1989], and the Chicxulub impact is believed to have been at 20 to 30 degrees from horizontal [Schultz and D'Hondt, 1996]. Based on this information, the base simulation contained a 5-km (in diameter) meteor impacting vertically with a 40-km/s velocity. This vertical impact was used for the base scenario so that the asymmetric results from angled impacts could be compared later. Using this simulation as the base, an array of simulations (Table 3.1) was designed to determine the effects of speed, angle, size, and location.

Table 3.1 Meteor simulation array

| Simulation | Speed (km/s) | Diameter (km) | Impact Angle (degrees from horizontal) | Location (km) |
|-------------------|-------------------------|--------------------------|--|--|
| Base | 40 | 5 | Vertical | Plate Boundary |
| Speed | 10 70 | 5 | Vertical | Plate boundary |
| Size | 40 | 1 3 7 9 | Vertical | Plate Boundary |
| Angle | 40 | 5 | 45 (going toward ocean) 45 (going toward continent) 80 (going toward ocean) 80 (going toward continent) 25 (going toward ocean) 25 (going toward continent) | Plate Boundary |
| Location | 40 | 5 | Vertical | 10 (left) 10 (right) 20 (left) 20 (right) |

In addition to these simulations, the base simulation was also calculated using the Bammann-Chiesa-Johnson (BCJ) viscoplastic/damage model for olivine's plasticity [Bell

et al., 2003]. Studies, like those by Regenauer-Lieb et al. [2001], have shown how water weakens mantle materials and creates an environment more susceptible to subduction initiation. To account for this weakening, the olivine layer in the oceanic plate is modeled as wet olivine, and the olivine layer in the continental plate is modeled as dry olivine. The BCJ material models for wet and dry olivine were taken from Horstemeyer [2006] and listed in Appendix A (Table A.2).

Gravity and boundary conditions were modeled carefully because they have great influence on lengthy large-scale simulations. The side boundaries and the boundary above the meteor were modeled as transmitting boundaries so that material could flow across the boundaries and no wave reflections would occur. The bottom boundary was constructed as a 100-km layer of spinel and a symmetric boundary beneath the spinel layer. The symmetric boundary condition was required so that gravity would not pull the entire model downwards. The symmetric boundary would have reflected the stress wave; so the spinel layer was added so that the reflection would not affect the 100-second simulation results. If the simulation were to be for more time, the reflected wave would alter the results. Even with this symmetry boundary, gravity was able to pull the Earth's layers down. To alleviate this problem, a pressure profile was applied throughout the depth; this pressure profile was equivalent to the pressure created by gravity.

The cell number for these simulations was minimized because the size and time were large. By limiting this model to two dimensions, the number of cells and equations per cell were significantly reduced. However, in reality, an impact at a boundary is a three-dimensional event. To determine the stress magnitude difference between two- and

three-dimensional simulations, the impact simulation, shown in Figure 3.3, was completed using two-dimensional and two-dimensional-circular meshing schemes. The two-dimensional scheme was modeled with symmetry about the y-axis; in this case, results were calculated as if the meteor were a cylinder. The circular meshing scheme calculated results as if the geometry were rotated around the y-axis; this circular meshing gave results as a three-dimensional model would with a spherical meteor. The displacement of 110-km deep tracers was compared for the two schemes using different meteor sizes as recorded in Table 3.2. Displacement as a function of meteor radius was found to be a second order polynomial for two-dimensional meshing and third order for two-dimensional-circular meshing. Using these results and relationships, the two-dimensional meteor size can be converted to three-dimensional size (see Table 3.3). Using the two-dimensional scheme with the base meteor simulation (Figure 3.2), mesh refinement was performed to minimize the number of cells necessary. The displacement of a 550-km deep tracer was compared for cell lengths of 0.5 km, 1 km, and 2 km; the results (Table 3.4) revealed that a 1-km mesh size was adequate.

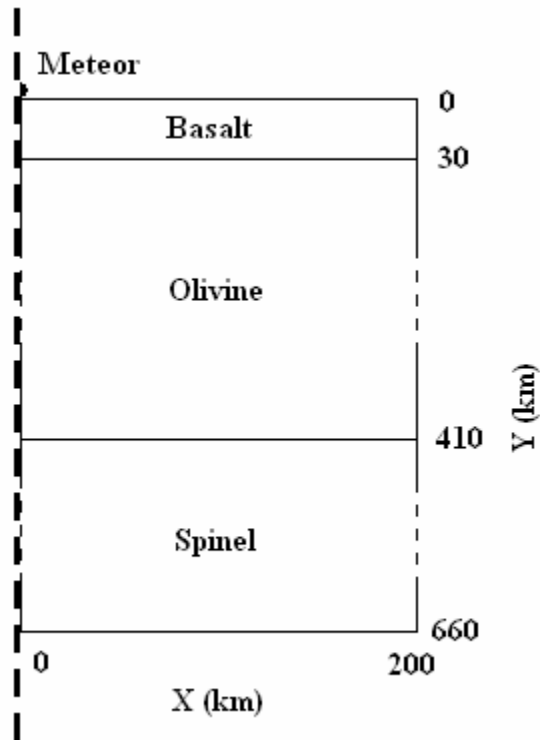


Figure 3.3 Two-dimensional meteor impact simulation for investigation of rectangular and circular meshing schemes

Table 3.2 Comparison of tracer displacements for rectangular and circular meshing schemes with different meteor sizes. The tracer was initially at (3km, -110km).

| | Rectangular Meshing | | | | | | Circular Meshing | | | | |
|--|--|-------|-------|-------|------|------|--|-------|------|------|-------|
| Meteor Radius (km) | 0.333 | 0.384 | 0.471 | 0.666 | 2.5 | 4.5 | 2.5 | 3.805 | 6.04 | 7.61 | 10 |
| Tracer Displacement (km) | 0.547 | 0.581 | 0.591 | 0.758 | 10.5 | 27.3 | 0.344 | 0.658 | 3.79 | 7.82 | 20.55 |
| Tracer Displacement as a function of Meteor Radius | $\text{Disp}(r) = 1.0414r^2 + 1.4024r$ | | | | | | $\text{Disp}(r) = 0.0318r^3 - 0.1421r^2 + 0.2841r$ | | | | |

Table 3.3 Two-dimensional meteor radius conversion to three-dimensional

| | | | | | |
|-----------------------|-----|-----|-----|-----|------|
| 2D Meteor Radius (km) | 0.5 | 1.5 | 2.5 | 3.5 | 4.5 |
| 3D Meteor Radius (km) | 4.1 | 6.4 | 8.1 | 9.6 | 10.9 |

Table 3.4 Cell length comparison using tracer displacement [initially at (10km, -550km)]

| Cell Length (km) | Tracer Displacement (m) | Difference Compare to Smallest Cell Length |
|------------------|-------------------------|--|
| 2 | 242 | 3.2 % |
| 1 | 248 | 0.8 % |
| 0.5 | 250 | -- |

Meteor Impact Results

Evaluation of the base simulation revealed the extremely high stresses induced by the impact. The pressure wave, which was on the order of gigapascals, traveled between 6 and 10 km/s, depending on the medium (see Figure 3.4). The pressure magnitude was monitored throughout the depths and displayed in Figure 3.5. The pressure increase was found by subtracting the gravity-induced pressure from total magnitude and was plotted in Figure 3.5 also. A small jump in the pressure increase was found at the 410-km depth; this jump was caused by refraction as the pressure wave entered the spinel region.

Between the depths of 400 and 660 km, the pressure increase was between 4 and 6.5 GPa; this increase surpasses the pressure increase (10 to 100 MPa) required for the mineralogical phase transitions. The shear stresses in this base simulation were inspected for possible shear banding. The shear stresses seemed to form in three stages as depicted in Figure 3.6. First, the shear stresses alternated, in direction, in and behind the pressure wave. The positive and negative stresses for this stage (time = 25s) are shown in Figure 3.6. Second, uniform shear formed on each side of the boundary once the pressure wave

had traveled sufficiently away from the impact area. Last, reversed shear appeared near the boundary as the material under the impact began to move upward. Evidence of shear banding was not seen, but this weakening could be possible given the high shear stresses sustained in such a large volume of earth.

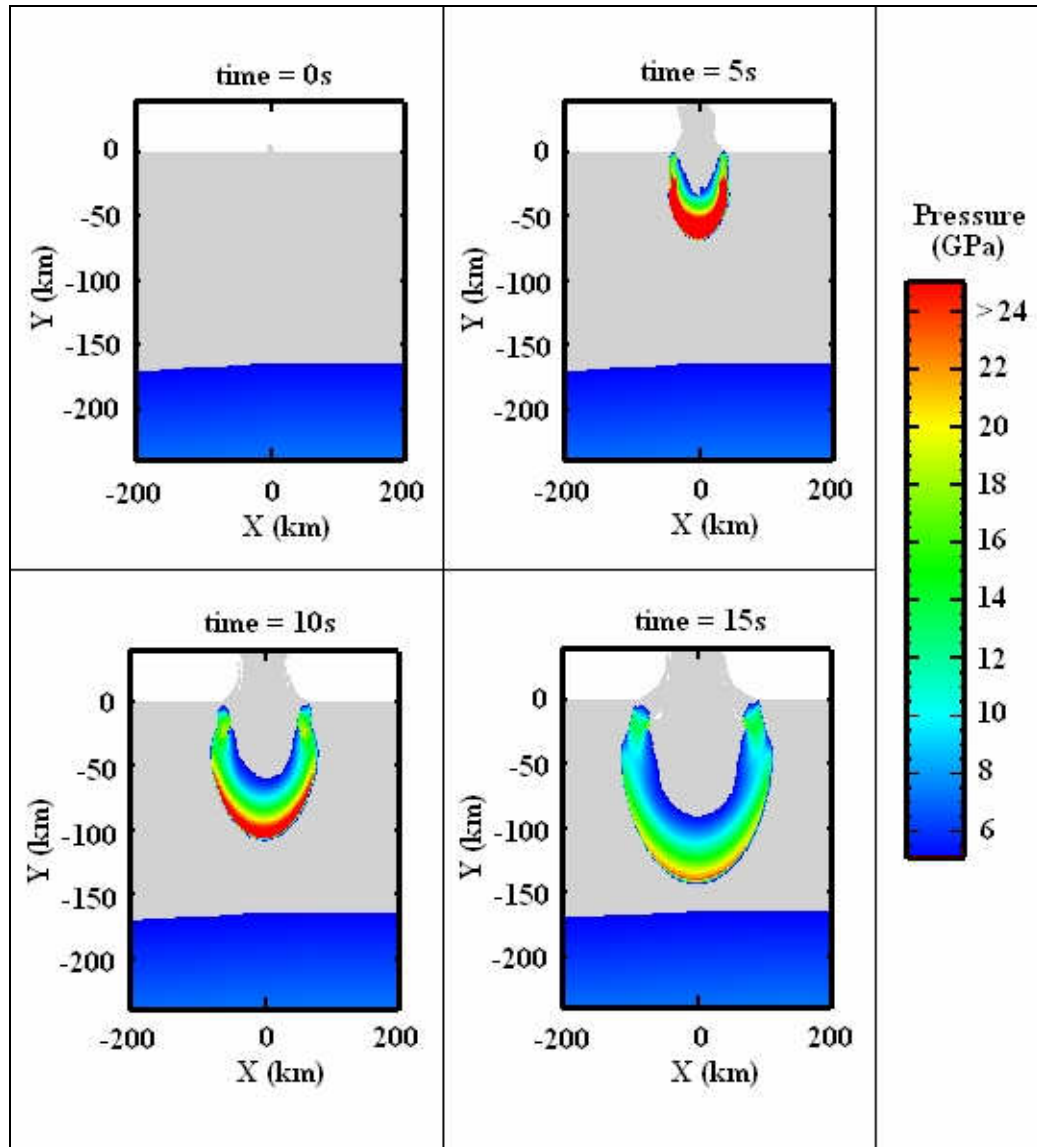


Figure 3.4 Pressure during the meteor impact simulation at 0, 5, 10, and 15 seconds after impact. This figure illustrates the stress wave decay as energy was absorbed by more of the Earth.

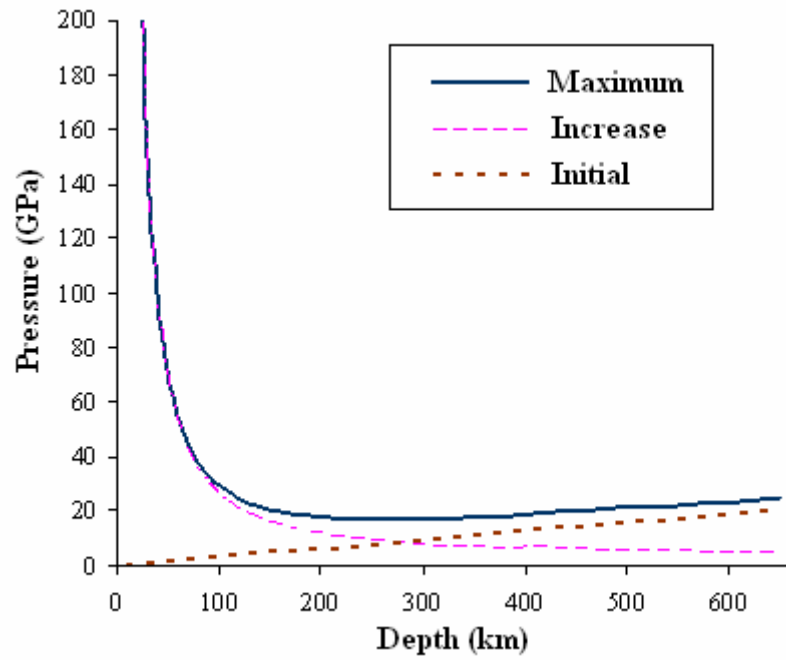


Figure 3.5 Initial and maximum pressure versus depth for the base meteor impact simulation. The pressure increase (difference between initial and maximum) illustrates pressure decay with depth.

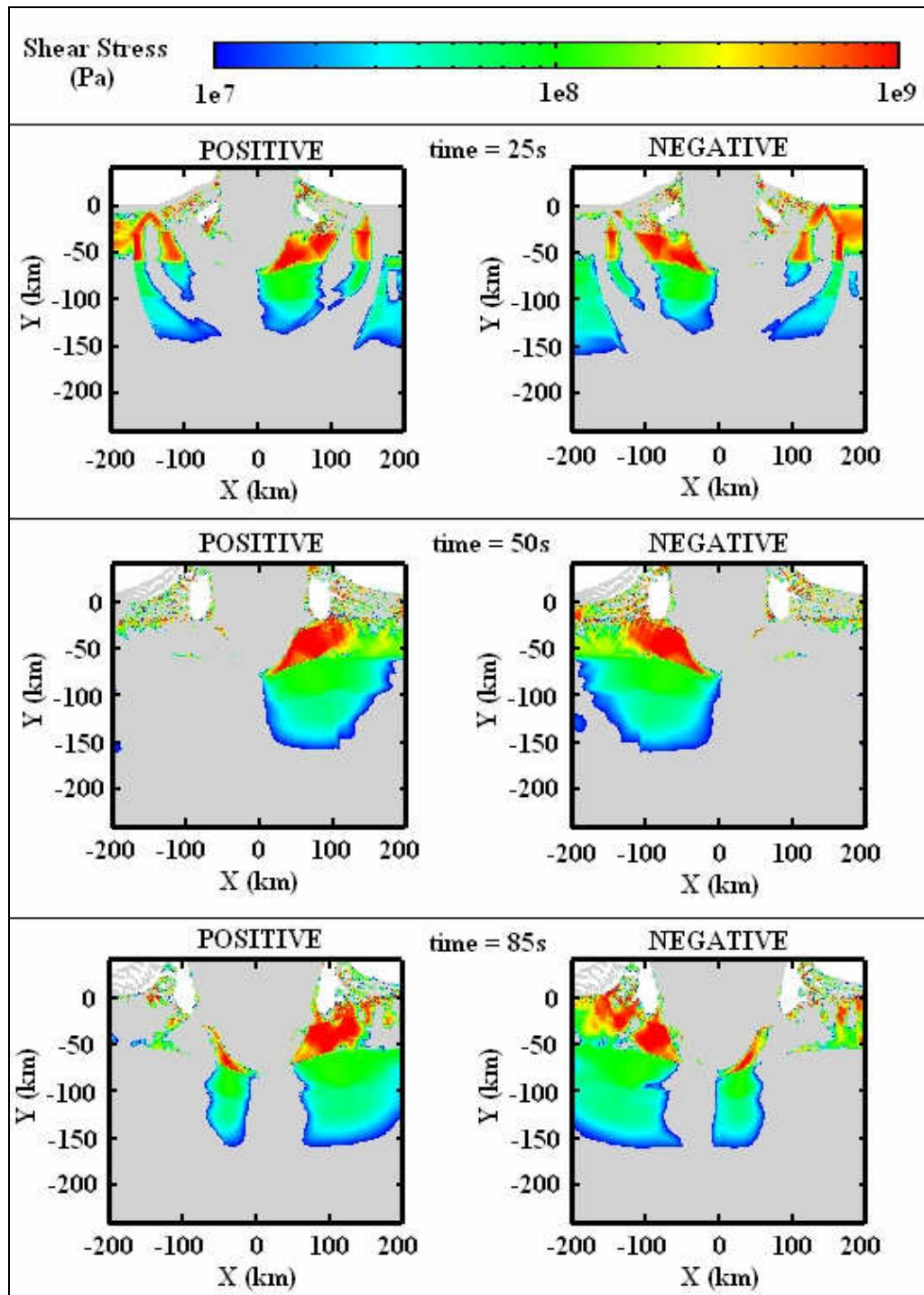


Figure 3.6 Positive and negative shear stress during the meteor impact simulation at 25, 50, and 85 seconds after impact. This figure illustrates the shear stress just behind the pressure wave (time = 25s), sustained uniform shear (time = 50s), and reversed shear caused by upward moving material (time = 85s).

Pressure increase was compared for the meteor speed and size parametric simulations. When the size or speed was varied, the pressure and shear stress contours followed the same patterns as described for the base simulation. Only the magnitudes differed significantly. The pressure increase throughout the Earth's depth was compared for the meteor size and speed variations. Figure 3.7 shows that the faster meteors transferred more kinetic energy to the Earth. Figure 3.8 shows that the larger meteors transferred more kinetic energy to the Earth. The meteor diameters listed are for the two-dimensional simulations; the three-dimensional diameters can be calculated from Table 3.2. For all of these simulations, the pressure increase was above the mineral phase transition criterion.

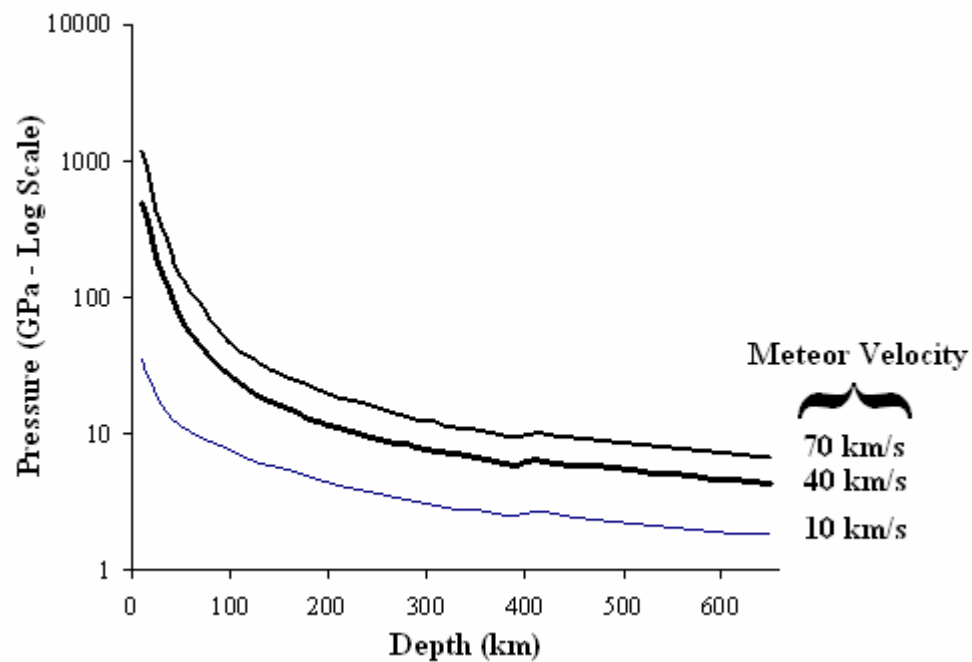


Figure 3.7 Maximum pressure increase in the Earth's depths due to 5-km meteor impacts of 10, 40, and 70 km/s

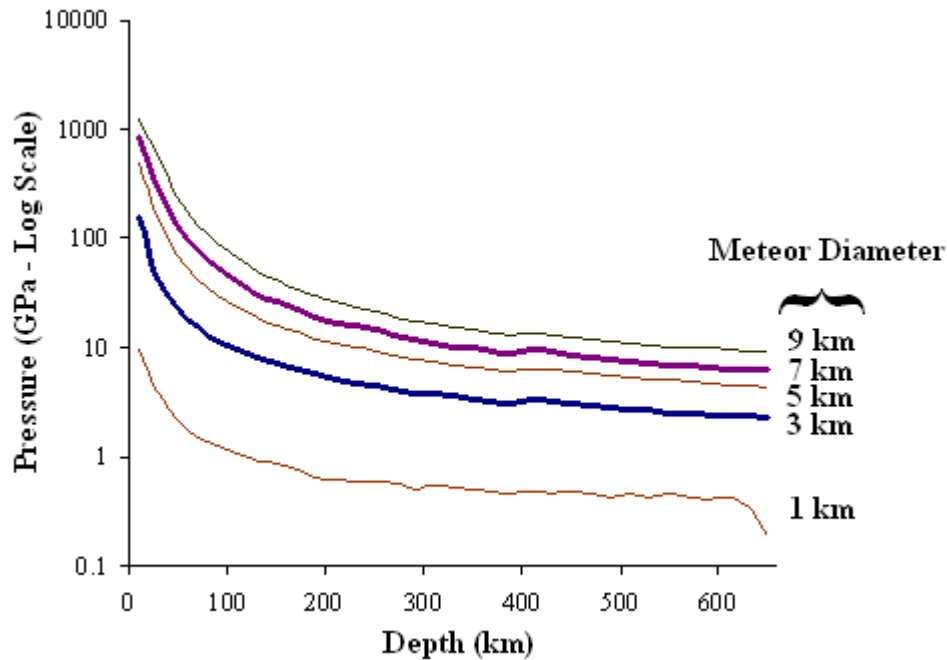


Figure 3.8 Maximum pressure increase in the Earth's depths due to 40-km/s impacts of 9-, 7-, 5-, 3-, and 1-km meteors. The three-dimensional meteor radii would be 21.8, 19.2, 16.2, 12.8, and 8.2 km.

Material displacement was compared for the impact angle and impact location parametric simulations. For these simulations, the pressure and shear stress contours, relative to the impact location, were consistent with the base simulation. The stress magnitudes did decrease with lower impact angles since less of the meteor's momentum was directed downward. Tracers, originally 5 km from the boundary, were monitored to show the material displacement due to differing impact angles and impact locations. For the impact angle variations, the tracers revealed that the material below the Earth's surface tended to travel opposite of the impact direction (see Figure 3.9). Meteors impacting toward the ocean sent material toward the continental plate, and meteors impacting toward the continent sent material toward the oceanic plate. For the impact

location variations, the tracers moved away from the impact location (see Figure 3.10).

As the impact location was moved away from the tracers, the tracer displacement becomes more uni-directional.

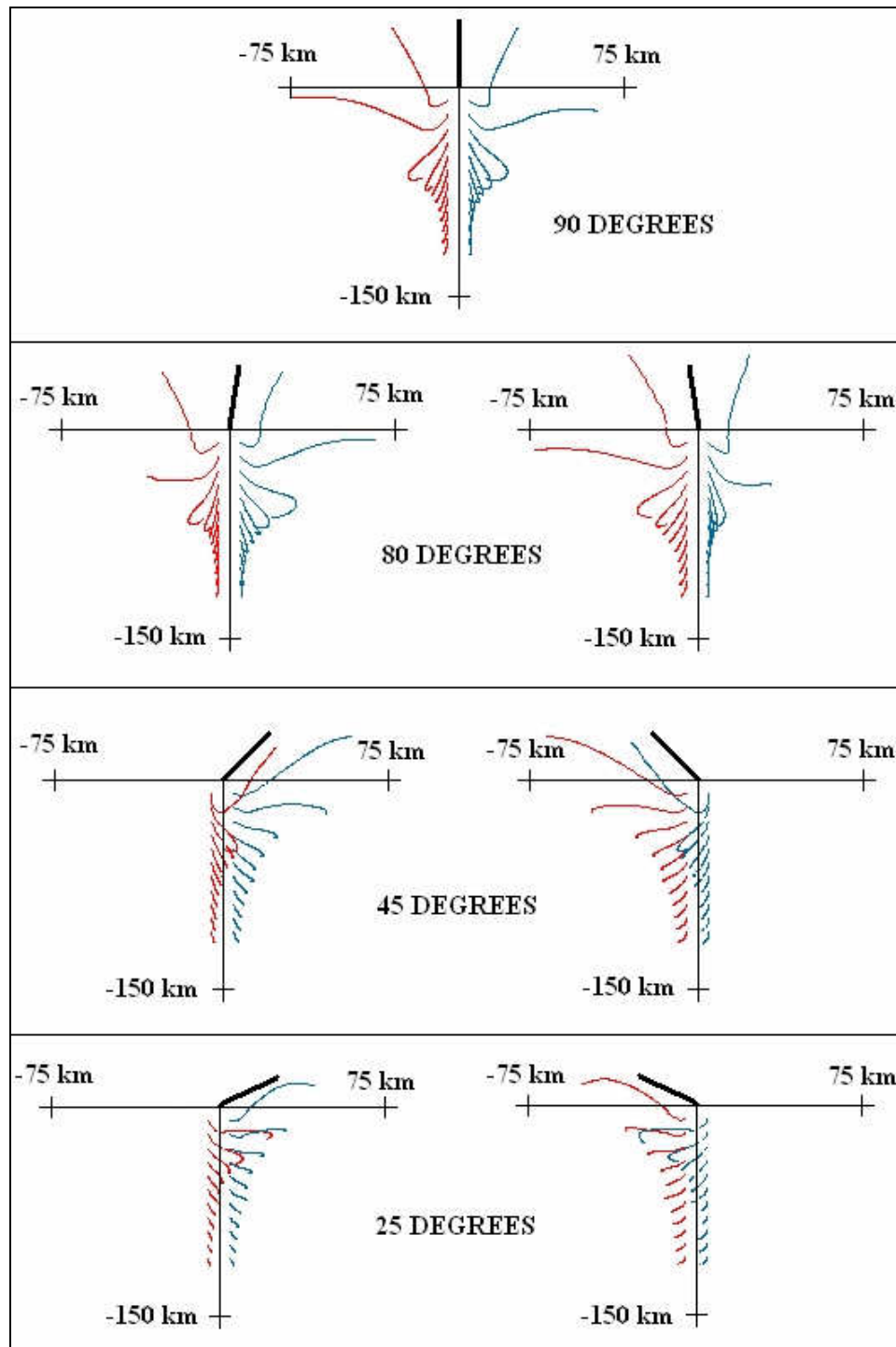


Figure 3.9 Tracer paths during meteor impacts at angles of 90, 80, 45, and 25 degrees from horizontal. The thicker line indicates the meteor's flight path. These tracers, originating 5 km from the boundary, illustrate how the material flow is opposite of the impact direction.

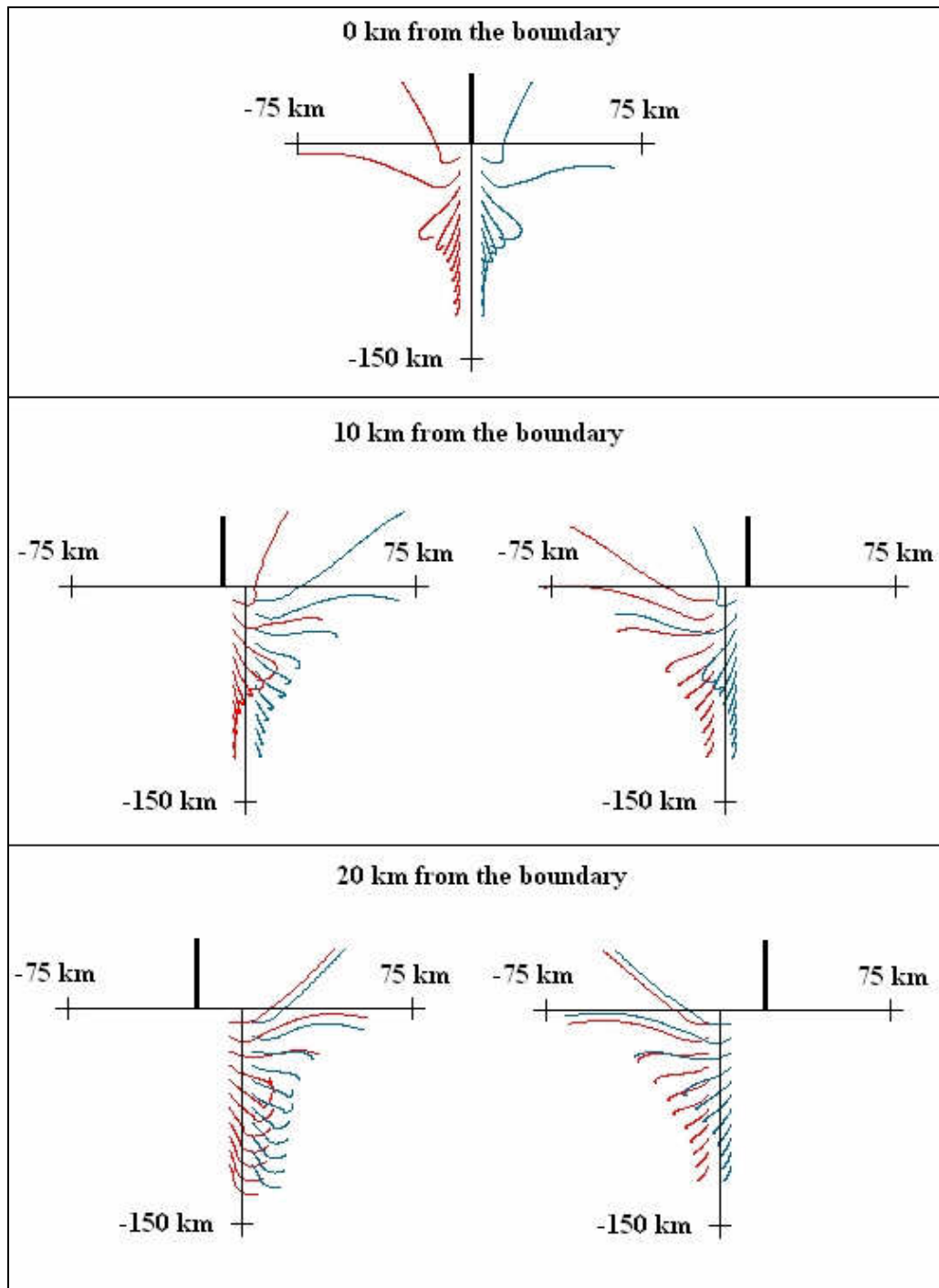


Figure 3.10 Tracer paths during meteor impacts at 0, 10 and 20 kilometers from the tectonic boundary. The thicker line indicates the meteor's flight path and impact location. These tracers, originating 5 km from the boundary, illustrate how the material at a boundary flowed by impact location.

Using the BCJ plasticity model for wet and dry olivine produced more asymmetric results when compared to the base simulation. In the base simulation, the olivine in the oceanic and continental plates differed only in density; their yield strengths were equal. The wet and dry olivine BCJ plasticity models used for this simulation did differ in their yield strengths. The wet olivine, used in the oceanic plate, was somewhat weaker than the dry olivine, used in the continental plate. The material displacement asymmetry was revealed by a tracer plot (Figure 3.11). The pressure wave traveling through the wet and dry olivine compared well with the base simulation. However, the shear stresses were greater and more asymmetric than the base simulation, as shown in Figure 3.12.

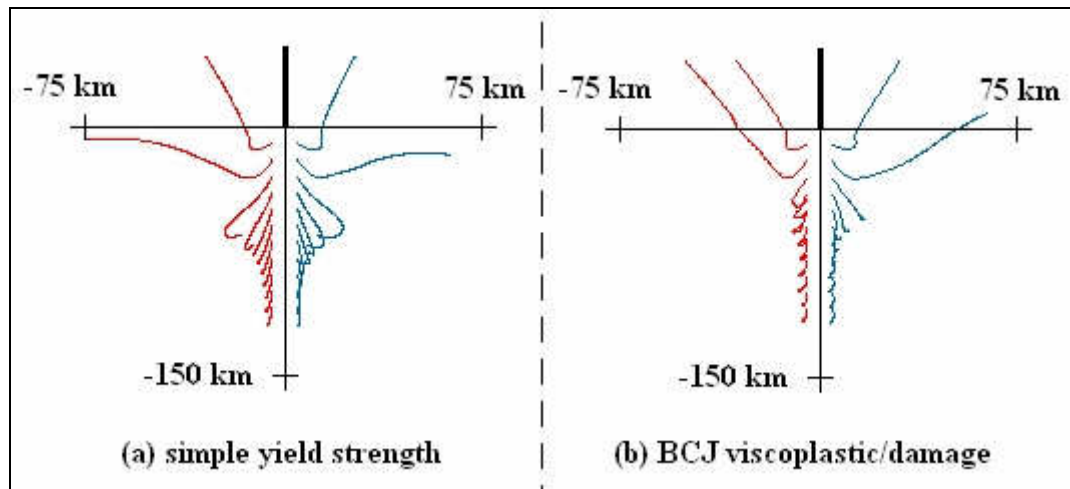


Figure 3.11 Tracer paths during meteor impacts using (a) simple yield strengths and (b) BCJ plasticity models for olivine. The thicker line indicates the meteor's flight path and impact location. The tracers originate 5 km from the boundary.

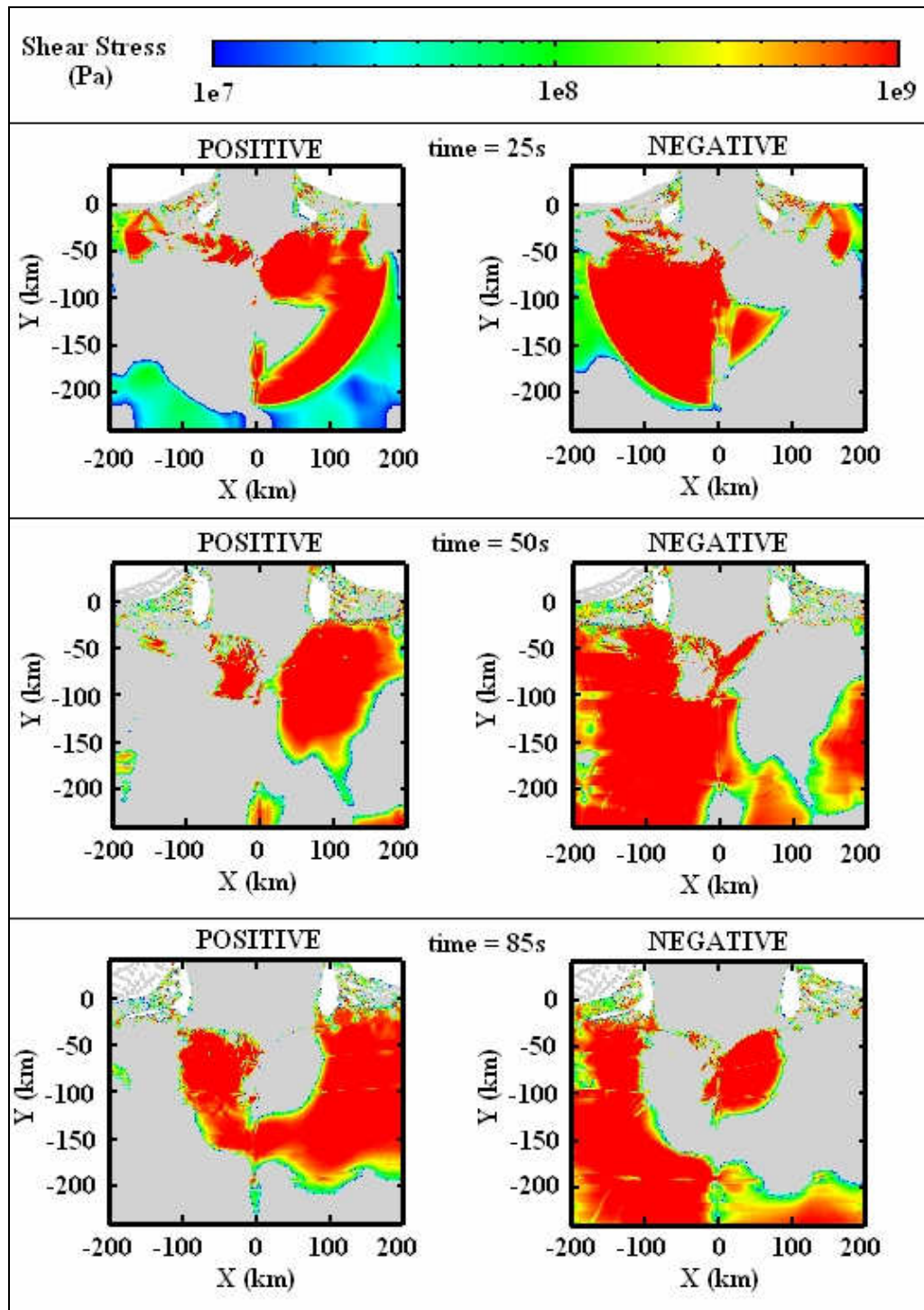


Figure 3.12 Positive and negative shear stress during the meteor impact simulation at 25, 50, and 85 seconds after impact using the BCJ plasticity model for wet and dry olivine. These shear stresses are greater and more asymmetric than the base simulation.

To evaluate the strain rate difference between the two plates, the plastic strain rate was recorded at tracers along the tectonic border. At no depth was the strain rate found to differ by two orders of magnitude. To illustrate the strain rate history, the plastic strain rate at a sixty-kilometer depth was plotted for both plates during the base meteor simulation (Figure 3.13). The plastic strain rate only differs slightly between the oceanic and continental plates. The plastic strain rate at the same location was plotted for the BCJ simulation (Figure 3.14). For the BCJ simulation, the strain rate differs between the oceanic and continental plates. However, the difference is not two orders of magnitude.

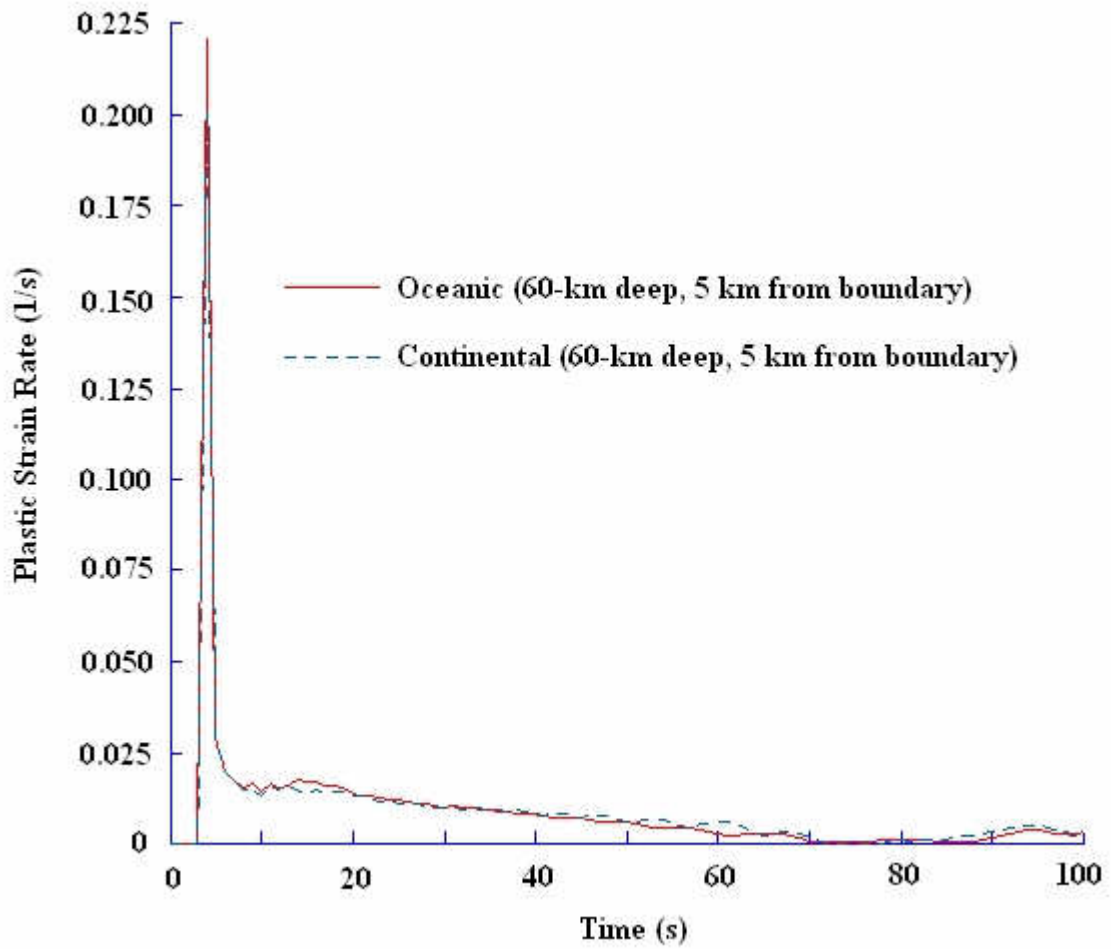


Figure 3.13 Plastic strain rate recorded at 60-km deep on each side of the tectonic boundary illustrating the similar strain rates in the base simulation

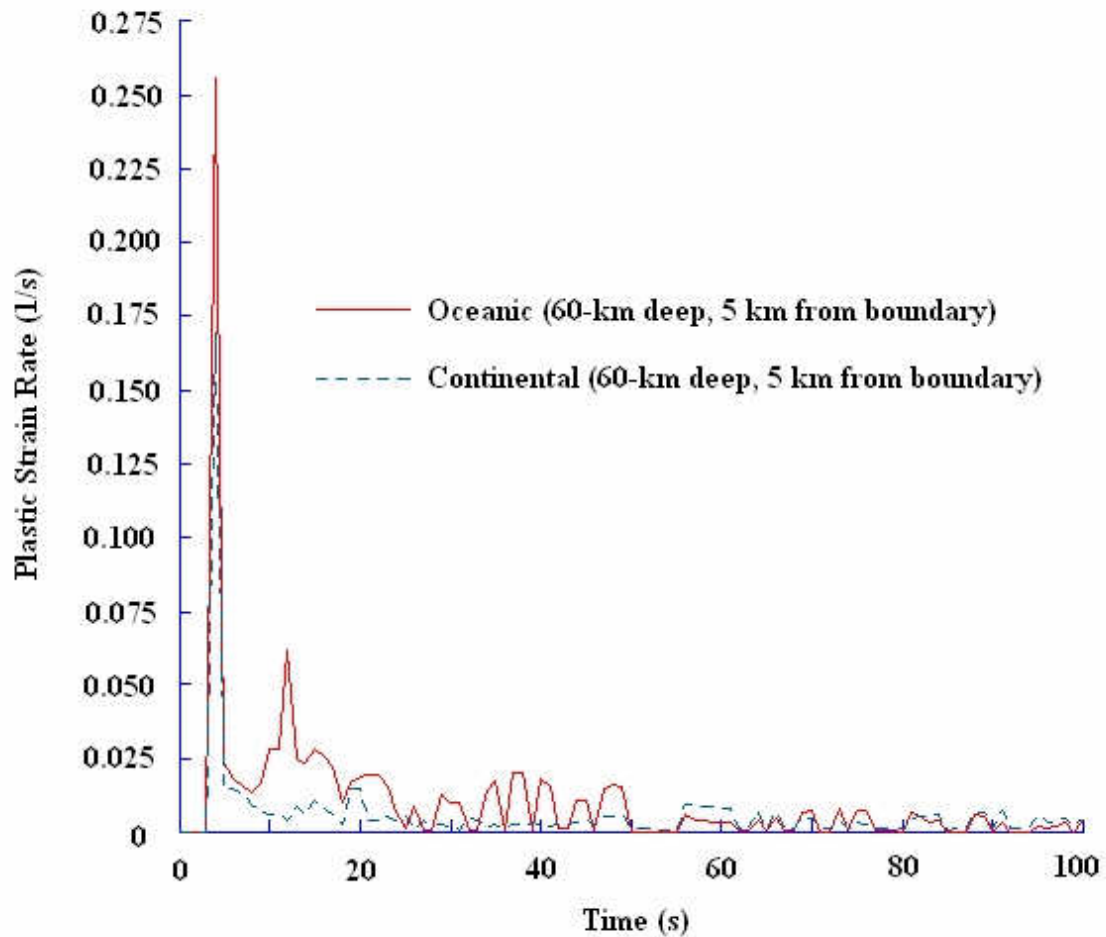


Figure 3.14 Plastic strain rate recorded at 60-km deep on each side of the tectonic boundary illustrating the slightly different strain rates in the BCJ-olivine simulation

Meteor Impact Conclusions

Large meteor impacts have more influence on the Earth's crust than just the craters they form. Through hydrocode modeling, the deeper effects of meteor impacts were shown. The intense pressure wave and shear stresses were capable of changing phases and yielding earth at large depths. The stress magnitude was dependent upon the meteor's size, velocity, and impact angle. The two-order strain-rate magnitude difference

was not found in the tectonic boundary. The initiation of subduction from meteoritic impact was not proven; however, the vast deformation and stress created by such an impact leads to subduction initiation being a possibility. A better understanding of material behavior deeper in the earth would increase the accuracy of these simulations.

REFERENCES

- Ahrens, T.J. and Johnson, M.L., "Shock Wave Data for Minerals," *Mineral Physics and Crystallography: A Handbook of Physical Constants* (edited by Ahrens, T.J.), American Geophysical Union, 143-184, 1995.
- Ahrens, T.J. and O'Keefe, J.D., "Impact on the Earth, Ocean and Atmosphere," *International Journal of Impact Engineering*, vol. 5, 13-32, 1987.
- Alvarez, L.W., Alvarez, W., Asaro, F., and Michel, H.V., "Extraterrestrial Cause for the Cretaceous-Tertiary Extinction," *Science*, vol. 208, 1095-1108, 1980.
- Anderson, O.L. and Isaak, D.G., "Elastic Constants of Mantle Minerals at High Temperature," *Mineral Physics and Crystallography: A Handbook of Physical Constants* (edited by Ahrens, T.J.), American Geophysical Union, 64-97, 1995.
- Bell, R.L., Baer, M.R., Brannon, R.M., Cole, R.A., Crawford, D.A., Elrick, M.G., Hertel, Jr., E.S., Silling, S.A., and Taylor, P.A., *CTH User's Manual and Input Instructions*, version 6.01, Albuquerque: Sandia National Laboratories, CTH Development Project, 2003.
- Collins, G.S., Melosh, H.J., Morgan, J.V., and Warner, M.R., "Hydrocode Simulations of Chicxulub Crater Collapse and Peak-Ring Formation," *Icarus*, vol. 157, 24-33, 2002.
- Hertel, Jr., E.S. and Kerley, G.I., *CTH Reference Manual: The Equation of State Package*, SAND98-0947, Albuquerque: Sandia National Laboratories, 1998.
- Hildebrand, A.R., Penfield, G.T., Kring, D.A., Pilkington, M., Zanoquera, A.C., Jacobsen, S.B., and Boynton, W.V., "Chicxulub Crater: A Possible Cretaceous/Tertiary Boundary Impact Crater on the Yucatan Peninsula," *Geology*, vol. 19, 9, 867-871, 1991.
- Horstemeyer, M.F., unpublished notes, 2007.
- Hutchison, R., *Meteorites: A Petrologic, Chemical and Isotopic Synthesis*, Cambridge University Press, 2004.
- Kious, W.J. and Tilling, R.I., *This Dynamic Earth: The Story of Plate Tectonics*, Washington, D.C.: U.S. Government Printing, 1996.
- Mason, B.H., *Meteorites*, New York: Wiley, 1962.

Melosh, H.J., *Impact Cratering: A Geologic Process*, New York: Oxford University Press, 1989.

O'Keefe, J.D. and Ahrens, T.J., "Impact-Induced Energy Partitioning, Melting, and Vaporization on Terrestrial Planets," *Proceedings of the Lunar Science Conference*, Eighth, 3357-3374, 1977.

Olivier, C.P., *Meteors*, Baltimore: Williams and Wilkins, 1925.

Pierazzo, E. and Collins, G., "A Brief Introduction to Hydrocode Modeling of Impact Cratering" in "Cratering in Marine Environments and on Ice," *Impact Studies* (edited by Henning, D., Burchell, M., and Claeys, P.), New York: Springer, 2003.

Pierazzo, E., Kring, D.A., and Melosh, H.J., "Hydrocode Simulation of the Chicxulub Impact Event and the Production of Climatically Active Gases," *Journal of Geophysical Research*, vol. 103, E12, 28607-28625, 1998.

Pierazzo, E. and Melosh, H.J., "Hydrocode Modeling of Chicxulub as an Oblique Impact Event," *Earth and Planetary Science Letters*, vol. 165, 163-176, 1999.

Price, N.J., *Major Impacts and Plate Tectonics*, New York: Routledge, 2001.

Regenauer-Lieb, K., Yuen, D.A., and Branlund, J., "The Initiation of Subduction: Criticality by Addition of Water?" *Science*, vol. 294, 578-580, 2001.

Schultz, P.H. and D'Hondt, S., "Cretaceous-Tertiary (Chicxulub) Impact Angle and Its Consequences," *Geology*, vol. 24, 11, 963-967, 1996.

Svetsov, V.V., "Numerical Simulations of Very Large Impacts on the Earth," *Planetary and Space Science*, vol. 53, 1205-1220, 2005.

Teterev, A.V., Nemtchinov, I.V., and Rudak, L.V., "Impacts of Large Planetesimals on the Early Earth," *Solar System Research*, vol. 38, 1, 39-48, 2004.

Wenk, H.-R., "The Texture of Rocks in the Earth's Deep Interior: Part II. Application of Texturing to the Deep Earth," *Encyclopedia of Materials: Science and Technology* (edited by Buschow, K.H.J., Cahn, R.W., Flemings, M.C., Ilshner, B., Kramer, E.J., Mahajan, S., and Veysiere, P.), Pergamon, 1-11, 2004.

CHAPTER 4
VALIDATION OF TENSION AND SHEAR SPECIMENS
UNDER DYNAMIC COMPRESSIVE LOADING

Introduction

High strain rate testing has become increasingly more important as materials are being selected for their high strain rate response. At these strain rates (100/s to 10000/s), Hopkinson techniques are the preferred means of mechanical testing [Nemat-Nasser, 2000]. The split Hopkinson pressure bar (SHPB) apparatus, first introduced by Kolsky [1949], operates by sending a pressure wave through the specimen; this pressure wave is created by launching the striker bar at the incident bar. The pressure wave passes through the incident bar and through the specimen which is held between the incident bar and the transmitter bar. Because the specimens are too small for strain gauges, the compressive force and deformation are calculated using strain gauge data from the incident bar and transmitter bar. Variations of the SHPB apparatus have been created for tension and torsion tests. [Al-Mousawi et al., 1997]

This chapter presents the evaluation of several SHPB specimens designed for shear and tensile deformation using the compressive SHPB apparatus. Validation and correct use of these specimens would allow for high-strain-rate shear, compression, and tension testing to be performed using the same piece of equipment. Also, this would

provide another method to retrieve shear and tensile data. For each specimen evaluated in this paper, finite element calculations were performed, and the gage section's stress state was compared to the specimen's proposed stress-strain calculation; if necessary, alterations to these calculations were proposed.

Proposed Hopkinson Techniques

Several SHPB specimens have been designed for tensile or shear deformation under compressive loading. Mohr and Gary [2007] presented the m-shaped specimen, shown in Figure 4.1, which is designed to produce, under compressive loading, tension in the gage section. The advantage of this design is that the specimen can be positioned freely between the incident and transmitter bars; conventional Hopkinson tensile techniques require the specimen to be gripped or threaded [Gray, 2000]. Gripping or threading can alter the test results. For this m-shaped specimen, Mohr and Gary [2007] presented equations used to determine the tensile response in the gage section using the force and deformation data taken from the incident bar and transmitter bar. The engineering stress and plastic strain in the gage section are calculated using

$$S_{yy}(t) = \frac{F(t)}{A_0} \quad (4-1)$$

$$E_{p_{yy}}(t) = \frac{u(t)}{l_{eff}} - \frac{F(t)}{K \cdot l_{eff}} \quad (4-2)$$

respectively, where $F(t)$ is the force recorded and A_0 is the total initial cross-sectional area of the two gage sections. The engineering plastic strain equation uses the height change $u(t)$, the effective length l_{eff} (assumed constant), and the entire specimen's

stiffness K. The true stress and true plastic strain are calculated using the conventional equations

$$\sigma_{yy} = (1 + E_{p_{yy}}) \cdot S_{yy} \quad (4-3)$$

$$\varepsilon_{p_{yy}} = \ln(1 + E_{p_{yy}}) \quad (4-4)$$

respectively. Mohr and Gary [2007] validated this specimen using quasi-static testing and two-dimensional static and dynamic finite element models; in these finite element models, they showed that a spacer block and base frame would reduce bending. Dynamic testing revealed repeatability. Mohr and Gary [2007] suggested that three-dimensional finite element simulations can be used to further validate and understand the loading response of this m-shaped specimen.

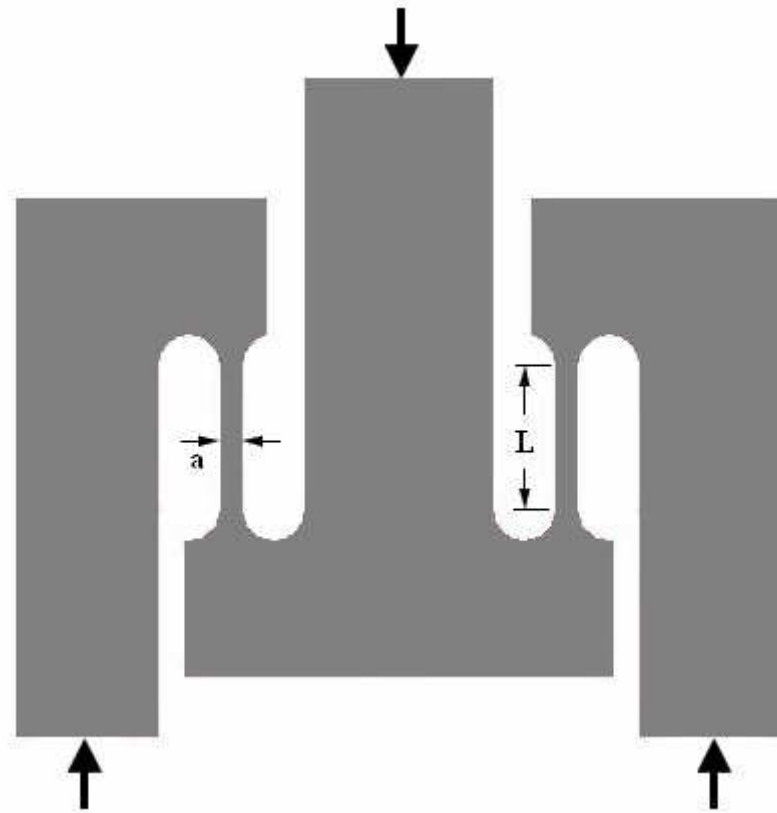


Figure 4.1 M-shaped specimen geometry presented by Mohr and Gary [2007] which is intended to produce tension in the gage section when compressed. The large arrows indicate compressive loading.

Rittel et al. [2002] presented a specimen, shown in Figure 4.2, in which, under compressive loading, the gage section undergoes shear and compression (mostly shear). This specimen is created by machining a notch in two sides of a cylinder; the notches are 45 degrees from the cylinder's longitudinal axis and are separated by the gage section. Rittel et al. [2002] have shown that the stress state in the gage section is three-dimensional and not simple shear or the ideal, pure shear; they proposed the following equations as approximates of the engineering equivalent stress and plastic strain:

$$\varepsilon_{eq} = \frac{u}{h} \quad (4-5)$$

$$\sigma_{eq} = 0.85 \cdot (1 - 0.2 \cdot \varepsilon_{eq}) \cdot \frac{F}{d \cdot t} \quad (4-6)$$

where ε_{eq} is the equivalent strain, σ_{eq} is the equivalent stress, u is the specimen height change, h is the gage height, F is the recorded force, d is the cylinder diameter, and t is the gage thickness. Equivalent stress-strain data, using this specimen in the SHPB apparatus, compares well with conventional compressive equivalent stress-strain data. The advantage of this specimen is that the gage height can be adjusted to obtain a wide range of strain rates; Rittel et al. [2002] reported experiments completed at strain rates of 47000/s and suggest that conventional testing frames can be used for strain rates of 1/s to 100/s.

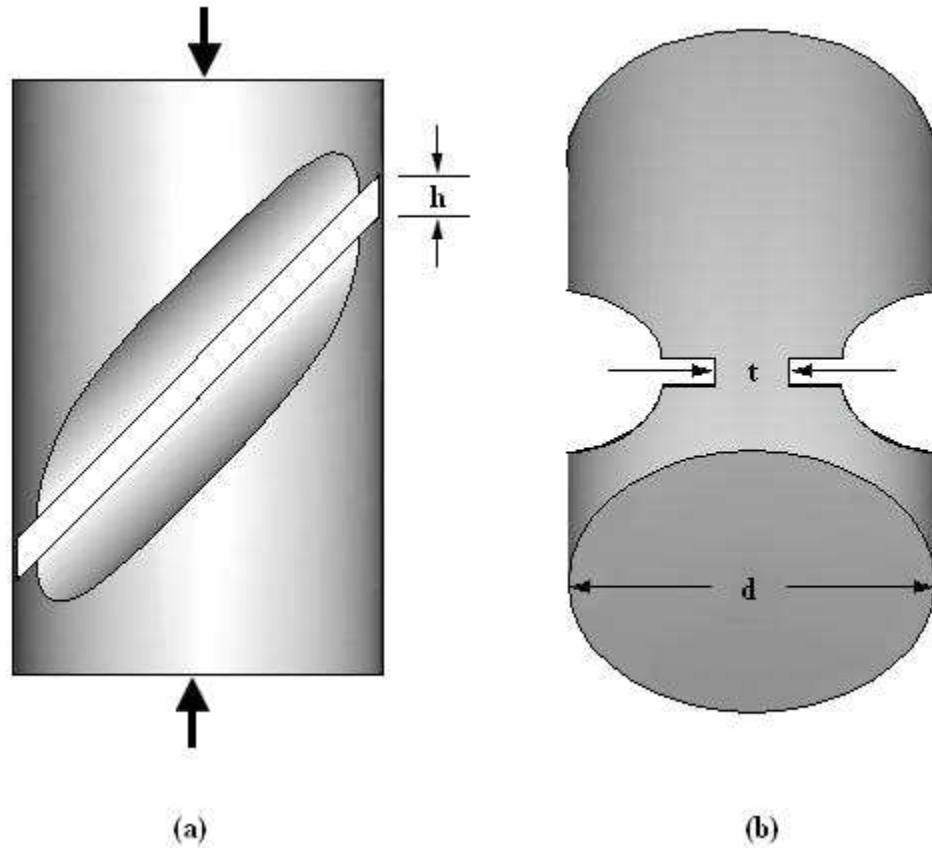


Figure 4.2 Shear-compression specimen presented by Rittel et al. [2002] where (a) is the side view and (b) is an angled view. This specimen is intended to produce shear in the gage section when compressed. The large arrows indicate compressive loading.

Hartmann et al. [1981] and Meyer and Kruger [2000] presented a hat-shaped specimen, shown in Figure 4.3, in which, under compressive loading, the gage section experiences dominant shearing. To produce this specimen, a cylinder is partially hollowed, and the groove is machined into the non-hollowed portion. Only a small band is retained between the two portions. This hat-shaped design is advantageous because a spacer ring may be placed in the groove to stop the experiment at a desired deformation. The following mean shear stress and strain equations for the gage section was proposed:

$$\tau = \frac{F}{\pi \cdot h \cdot \left(\frac{d_i + d_e}{2} \right)} \quad (4-7)$$

$$\gamma = \frac{u}{x} \quad (4-8)$$

where τ is the shear stress, γ is the shear strain, F is the recorded force, h is the height of the shear area in the axial direction, d_i is the diameter of the hollowed area, d_e is the diameter of the grooved area, u is the specimen axial deformation, and x is the shear area width $\{(d_e - d_i) / 2\}$. The shear strain equation (4-8) is based on the assumption that all axial deformation is in the shear area.

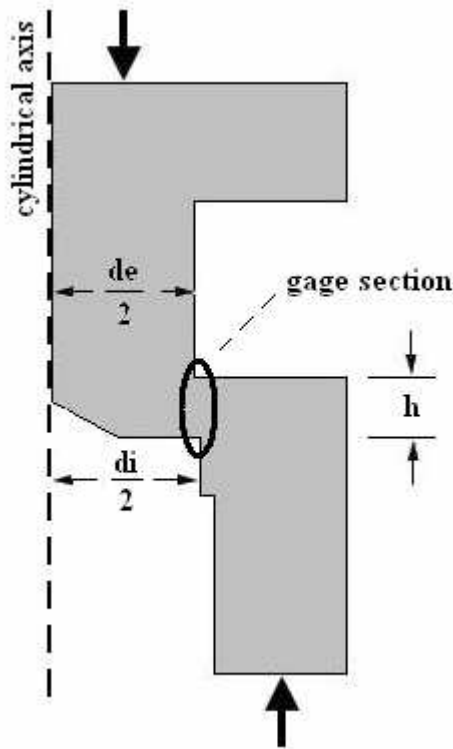


Figure 4.3 Hat-shaped specimen presented by Meyer and Kruger [2000]. This cross section is rotated about the cylindrical axis. This specimen is intended to produce shear in the gage section when compressed. The large arrows indicate compressive loading.

Finite Element Validation

To test the validity of these specimens at high rates, three-dimensional explicit finite element calculations were performed. For each specimen type, the finite element model was loaded as would be expected from the SHPB apparatus and given strain rates of at least 500/s. The incident bar is modeled as a 10.6-kg rigid plane and given an initial velocity; the transmitter bar is modeled as a 6.6-kg rigid plane and given no initial velocity. The force and displacement results as would be taken from the SHPB apparatus were recorded and used in the given stress and strain equations (4-1 through 4-8). These

stress-strain results are then compared to the stress-strain results in the respective gage sections. The calculations were performed using the LS-DYNA finite element software [Livermore Software Technology Corporation, 2003]. The material model used for each specimen, the aluminum alloy Al 6061-T6, was incorporated using the temperature-dependent and strain-rate-dependent plasticity model developed by Bammann [1990]; the material constants were taken from Guo et al. [2005] and listed in the Appendix (Table A.3).

M-Shaped Specimen

The m-shaped specimen proposed by Mohr and Gary [2007] was modeled with a 0.5-mm gage width (a in Figure 4.1), a 2.2-mm gage length (L in Figure 4.1), and a 28.3-mm specimen depth. Only a quarter model was necessary because of symmetry. Simulations were completed using initial incident plate velocities of 1.72 m/s and 6.87 m/s, which produced 660/s and 1050/s average strain rates respectively in the gage section. The simulation was constructed initially with only frictional boundary conditions and was then altered, with the addition of the spacer block and base frame to prevent bending, as proposed by Mohr and Gary [2007]. Figure 4.4 displays the difference in deformation. All subsequent hat-shaped simulations were constructed with these boundary conditions.

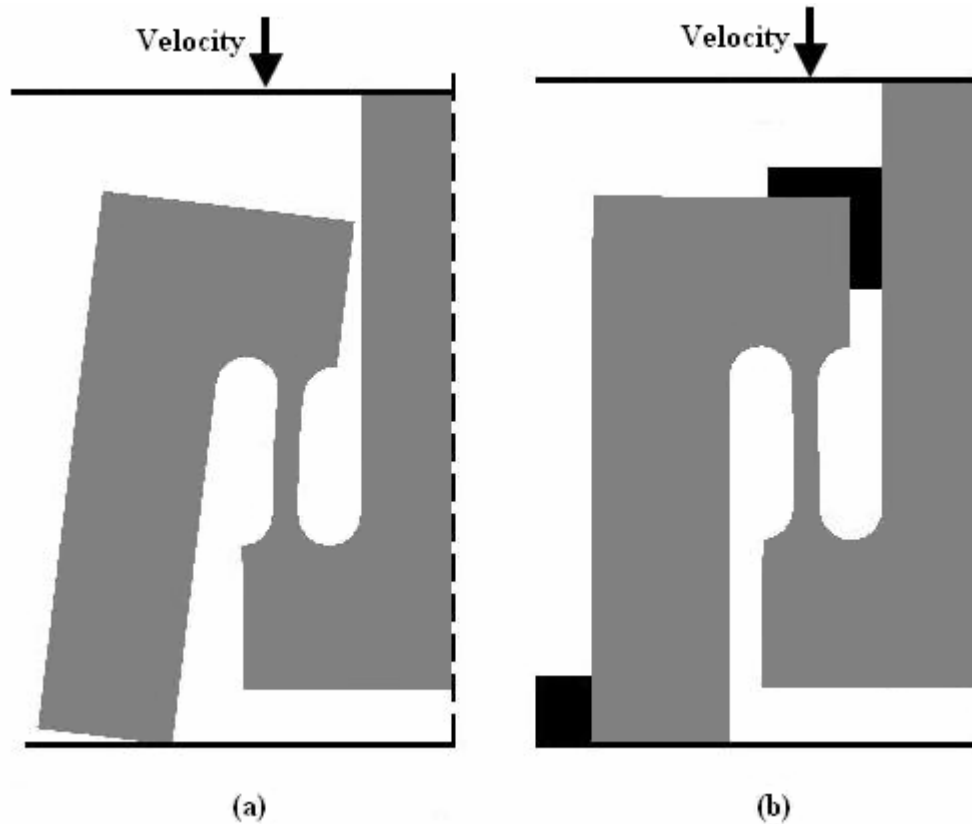


Figure 4.4 Deformation of the m-shaped specimen (time = 0.11 ms) (a) with friction applied at ends and (b) with the spacer block and base frame proposed by Mohr and Gary [2007]. Both simulations started with the same incident wall velocity.

The stress distribution found in this specimen was influenced by the bending forces. Figure 4.5a shows the uniaxial stress in the gage section when the specimen first experiences loading. From bending effects, the uniaxial stress was greatest in the top-left and bottom-right corners of the gage section. As the specimen deformed more, this bending force effect was masked by the greater tensile force, as shown in Figure 4.5b.

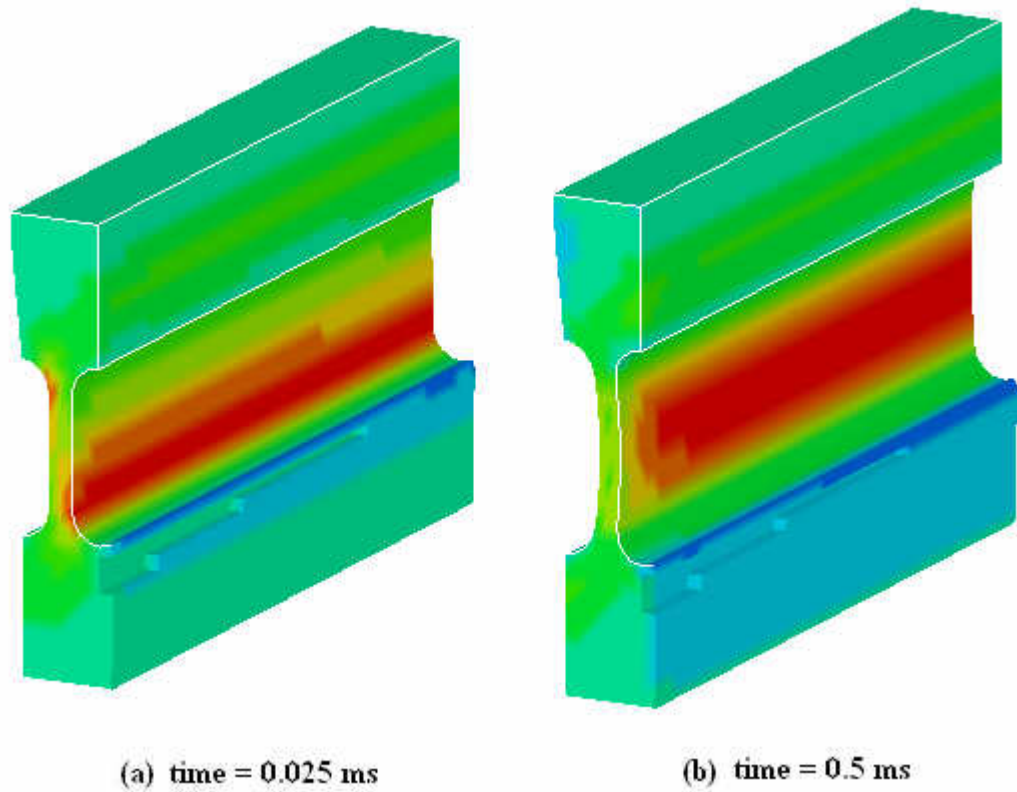


Figure 4.5 Uniaxial stress distribution in the m-shaped specimen's gage section taken from the finite element simulation. The front edge is the free edge, and the opposite edge is the symmetry border.

To validate this specimen's results, the recorded uniaxial stress and strain in the gage section were compared with calculations by Mohr and Gary [2007]. Stress and plastic strain were recorded in the middle of the gage section on the depth's symmetrical plane and displayed in Figure 4.6. The force and displacement of the specimen ends were recorded and used in the calculations proposed by Mohr and Gary [2007]. For these calculations, the specimen stiffness, K , was determined by a static finite element calculation, where a 0.015-mm compressive displacement was applied. The reaction force and subsequent stiffness was 641.9 N and 42.791 kN/mm, respectively. This

calculated stress-strain relationship was also plotted in Figure 4.6. Reflections of the stress wave in this specimen gave the results a rough appearance. The calculated stress-strain relationship agreed well with the recorded gage section up to a 0.1 strain. This process was repeated for the faster velocity, and the results were similar, as shown in Figure 4.7. For comparison, a single tensile element was modeled with the calculated strain history under free and plane strain boundary conditions; these results are also shown in Figure 4.6. These stress values are lower than those recorded in the specimen; this discrepancy alluded to the more complex stress state in the gage section. For example, at the location of the recorded stress and strain (time = 0.5ms), the following tensile stresses existed: 736 MPa in the intended tensile direction, 512 MPa in the depth direction, and 291 MPa in the gage width direction (negligible shear stresses). For further comparison, the results for a simple tension experiment were plotted in Figure 4.6 [Johnson and Holmquist, 1989]. This simple tension experiment was performed using a tension Hopkinson apparatus with a standard tensile specimen (622/s). The experimental stress level is also lower than the m-shaped results.

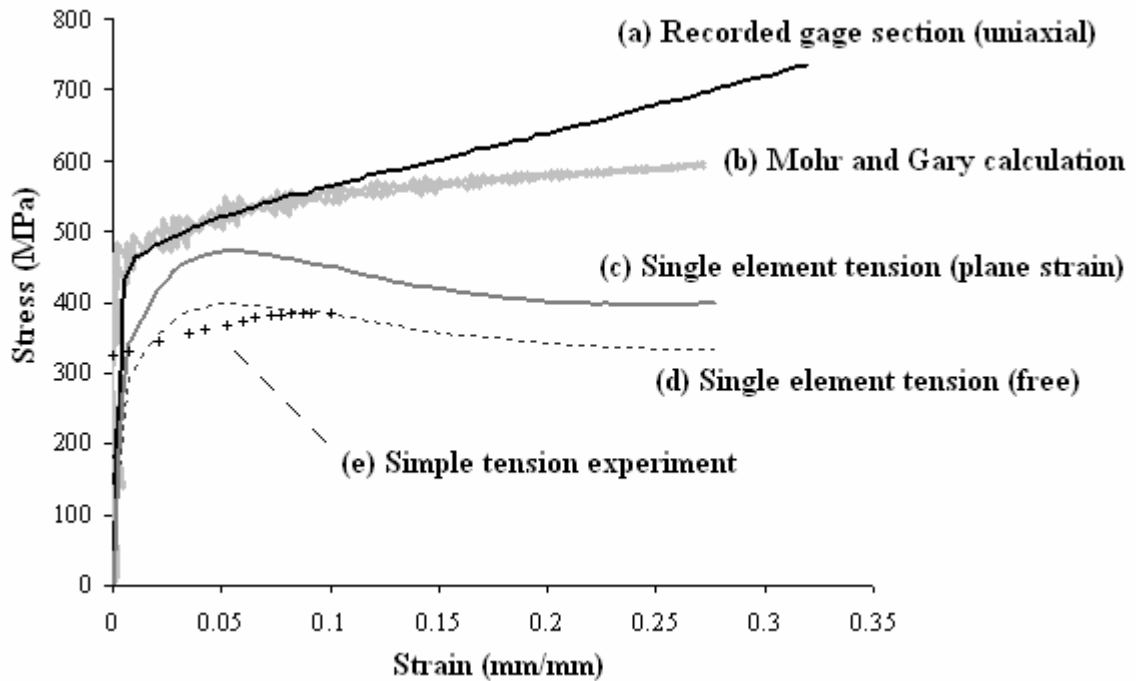


Figure 4.6 Finite element uniaxial stress-strain results for the m-shaped specimen ($\sim 600/s$) from (a) the gage section and (b) calculations using end force and displacements [Mohr and Gary, 2007]. The (a) curve is the uniaxial stress-strain relationship in the gage section, and the (b) curve is the approximate which would be calculated from experimental data. The strain history from (b) was used to deform a single element under (c) plane strain conditions and (d) free conditions. The stress-strain curve (e) for a simple tension experiment (622/s) [Johnson and Holmquist, 1989] has a much lower stress than the m-shaped results.

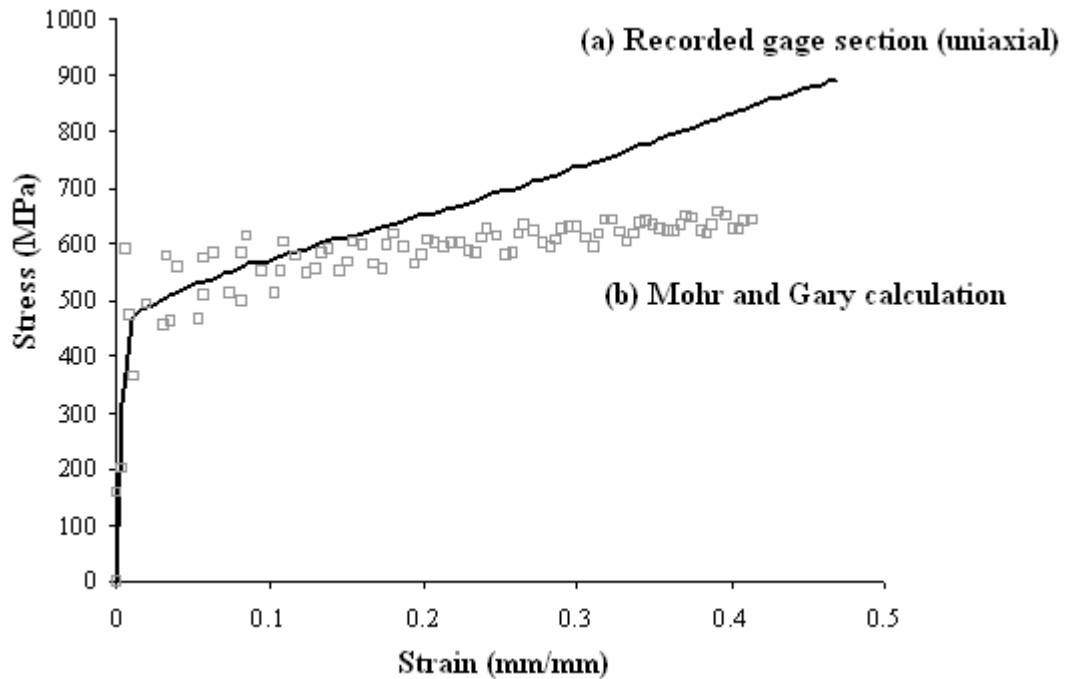


Figure 4.7 Finite element uniaxial stress-strain results for the m-shaped specimen (~1500/s) from (a) the gage section and (b) calculations using end force and displacements [Mohr and Gary, 2007]. The higher rate produced more fluctuation in the results compared to Figure 4.6.

Shear-Compression Specimen

The shear-compression specimen was modeled with a 1.27-mm gage height (h in Figure 4.2), a 2.54-mm gage thickness (t in Figure 4.2), a 12.54-mm diameter (d in Figure 4.2), and a 20-mm specimen height, as constructed for the experiment by Rittel et al. [2002]. Only a half model was necessary because of symmetry. Simulations were completed using an initial incident plate velocity of 2.0 m/s, which produced a 1990/s recorded shear strain rate and an 1170/s calculated equivalent strain rate. Figure 4.8 shows the deformation after 0.5 ms had elapsed; Figure 4.8 is also a contour plot showing locations of plastic strain. The plastic strain was constrained to the gage section.

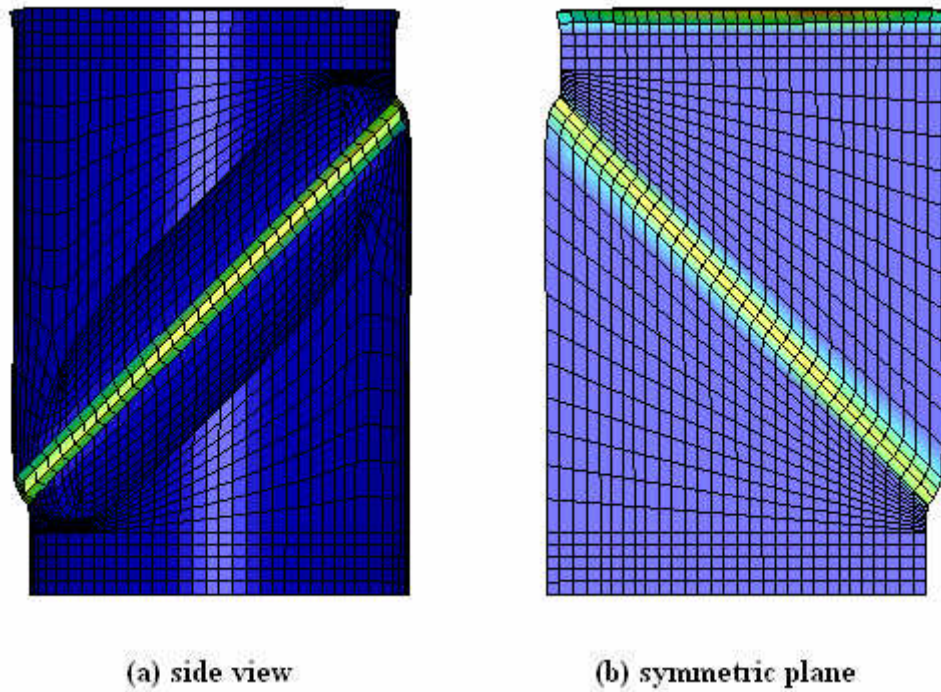


Figure 4.8 Plastic strain in the gage section of the Rittel et al. [2002] shear-compression specimen from the finite element simulation

To validate this specimen's results, the recorded equivalent stress and strain in the gage section were compared with the calculations proposed by Rittel et al. [2002]. Equivalent stress and equivalent plastic strain were recorded in the middle of the gage section on the symmetrical plane and are displayed in Figure 4.9. The force and displacement of the specimen ends were recorded and used in the calculations proposed by Rittel et al. [2002]. The calculated stress-strain relationship was also plotted in Figure 4.9. The calculated and recorded equivalent stress-strain curves agreed well for the yield strength magnitude, the ultimate strength magnitude, and, after 0.2 strain, the overall relationship.

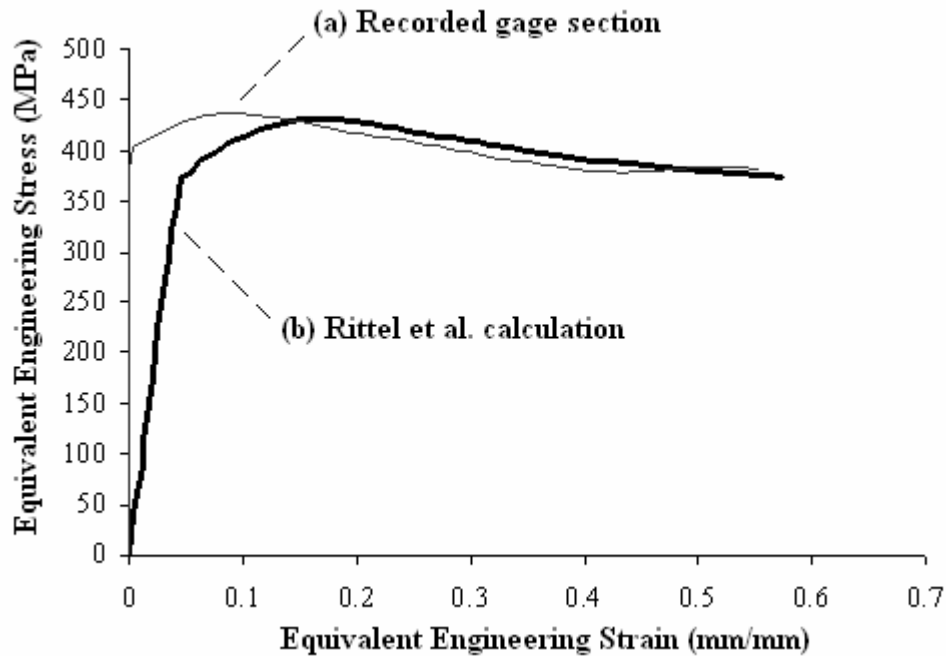


Figure 4.9 Equivalent stress-plastic strain results ($\sim 1400/s$) for the Rittel et al. [2002] shear-compression specimen (a) recorded in the gage section and (b) calculated from end force and displacements. These results are from the finite element simulation.

To determine this specimen's ability to capture shear stress-strain data, the recorded shear stress and strain in the gage section were compared with shear results calculated using the specimen's stiffness. The specimen's stiffness was determined by a static finite element calculation in which the gage section was removed and replaced by rigid boundary conditions. A 5000-N applied load resulted in a 0.043-mm compression; so the stiffness, K , of the specimen's non-gage portions was 115.12 kN/mm. The following shear strain and shear stress equations were derived assuming only simple shear deformation in the gage section which remains at a 45-degree angle to the applied load:

$$\gamma = 2 \cdot \frac{\Delta H - \frac{F}{K}}{h} \quad (4-9)$$

$$\tau = \frac{F}{2 \cdot d \cdot t} \quad (4-10)$$

where ΔH is specimen height change, h is the gage height, d is the cylinder diameter, t is the gage thickness, and F is the end force. The recorded and calculated shear stress-strain curves are shown in Figure 4.10. The discrepancy between the two curves was due to the compression that occurred in the gage section.

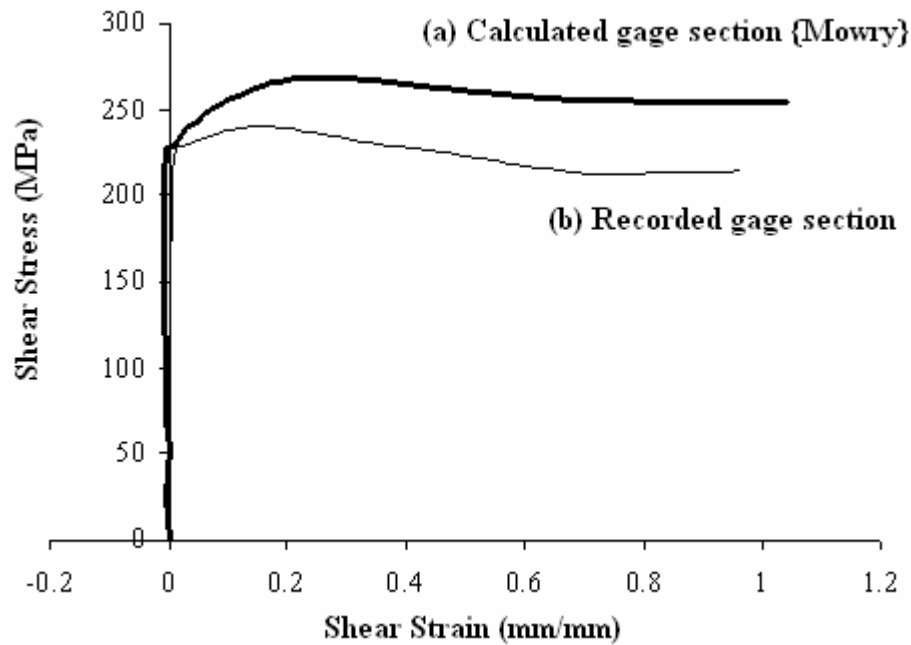


Figure 4.10 Shear stress-strain results ($\sim 2500/s$) for the Rittel et al. [2002] shear compression specimen (a) calculated from end force and displacements and (b) recorded in the gage section. These results are from the finite element simulation.

Hat-Shaped Specimen

The hat-shaped specimen was modeled with a 5.0-mm internal diameter (d_i in Figure 4.3), a 4.8-mm external diameter (d_e in Figure 4.3), a 1.0-mm gage height, a 0.1-mm gage width, a 10.0-mm total diameter, and a 10.0-mm total height. Because this specimen is symmetrical around the cylindrical axis, only a small piece needed to be modeled; for easy boundary condition application, a quarter of the specimen was modeled. Simulations were completed using an initial incident plate velocity of 150 mm/s, which produced a 550/s recorded shear strain rate. Figure 4.11 shows the stress contours of the deformed specimen after 0.6 ms. The shear stress (Figure 4.11a) was dominant in the gage section, as intended; however, compressive stresses (negative values in Figure 4.11b) leads to deformation in other areas of the specimen.

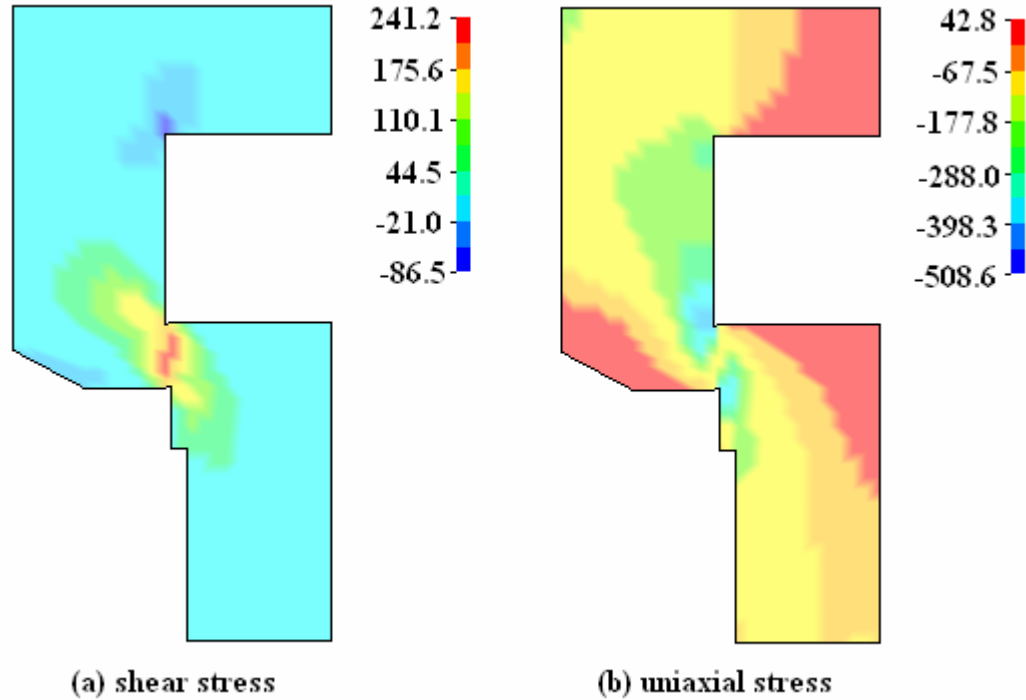


Figure 4.11 Stress contour plot of hat-shaped specimen cross section as calculated by the finite element simulation (time = 0.6 ms)

To validate this specimen's results, the recorded shear stress and strain in the gage section were compared with the calculations proposed by Meyer and Kruger [2000]. Shear stress and strain were recorded in the middle of the gage section and displayed in Figure 4.12. The force and displacement of the specimen ends were recorded and used in the calculations proposed by Meyer and Kruger [2000]. The calculated stress-strain relationship was also plotted in Figure 4.12. The calculated and recorded shear stresses agreed well because all of the compressive force is balanced in the shear zone. However, the shear strains did not agree; this discrepancy occurred because the compression of the non-gage sections was not considered. The stiffness of the non-gage sections was then

used to account for the non-gage deformation. The specimen's non-gage stiffness was determined by a static finite element calculation, in which the gage section was removed and replaced by rigid boundary conditions. A 700-N applied load resulted in a 0.0223-mm compression; so the stiffness K of the specimen's non-gage portions was 31.45 kN/mm for the quarter model, or 125.79 kN/mm for the whole specimen. For this geometry and a 0.33 Poisson's ratio, the stiffness of the non-gage sections is the modulus of elasticity times 1.8214 mm. The following shear strain equation was derived, assuming only simple shear deformation in the gage section:

$$\gamma = \frac{\Delta H - \frac{F}{K}}{w} \quad (4-11)$$

where ΔH is the specimen's height change, F is the compressive force, and w is the gage width. The strain calculated using this equation produced the curve (b) in Figure 4.12, which agreed well with the recorded strain.

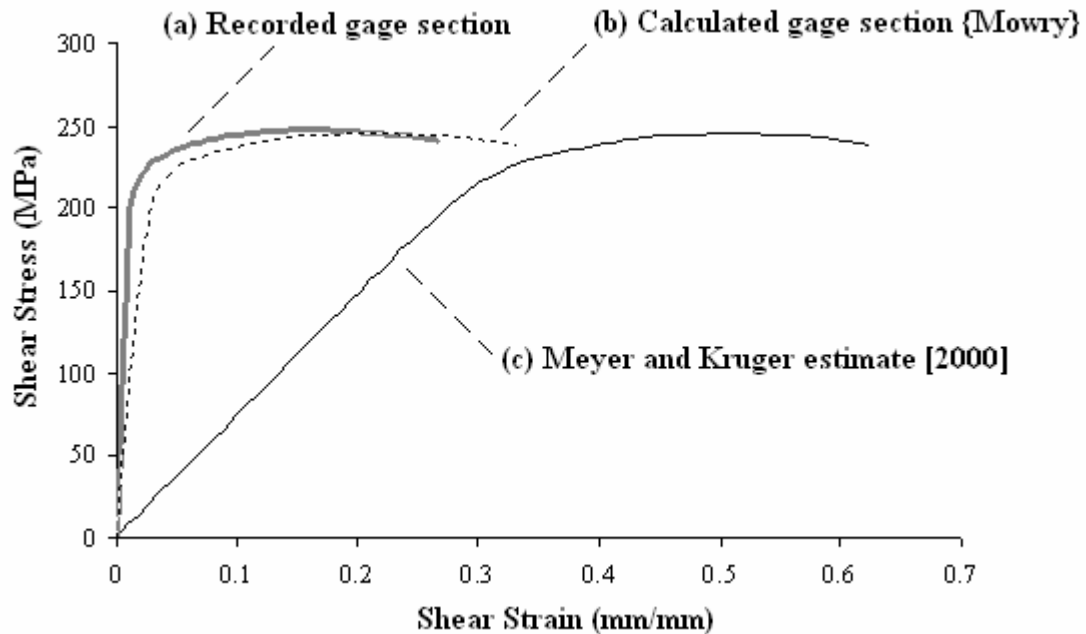


Figure 4.12 Shear stress-strain results ($\sim 750/s$) for the hat-shaped specimen (a) recorded in the gage section, (b) calculated from end force, end displacements, and specimen stiffness, (c) calculated assuming all displacement occurs in the gage section. These results are from the finite element calculation.

The shear stress-strain curve recorded in the gage section of the hat-shaped specimen compares well with that of the shear-compression specimen. The hat-shaped specimen test was simulated with a shear strain rate of approximately $2500/s$ for comparison with the shear-compression specimen test. A comparison of these two shear stress-strain curves (Figure 4.13) shows that the results are quite similar. The maximum shear stresses differed six percent. Shear stress and shear strain values from a dynamic torsion test ($232/s$) [Johnson and Holmquist, 1989] are slightly lower than the simulation results. The difference between the simulations' and the torsion experiment's stress is due to the different strain rates.

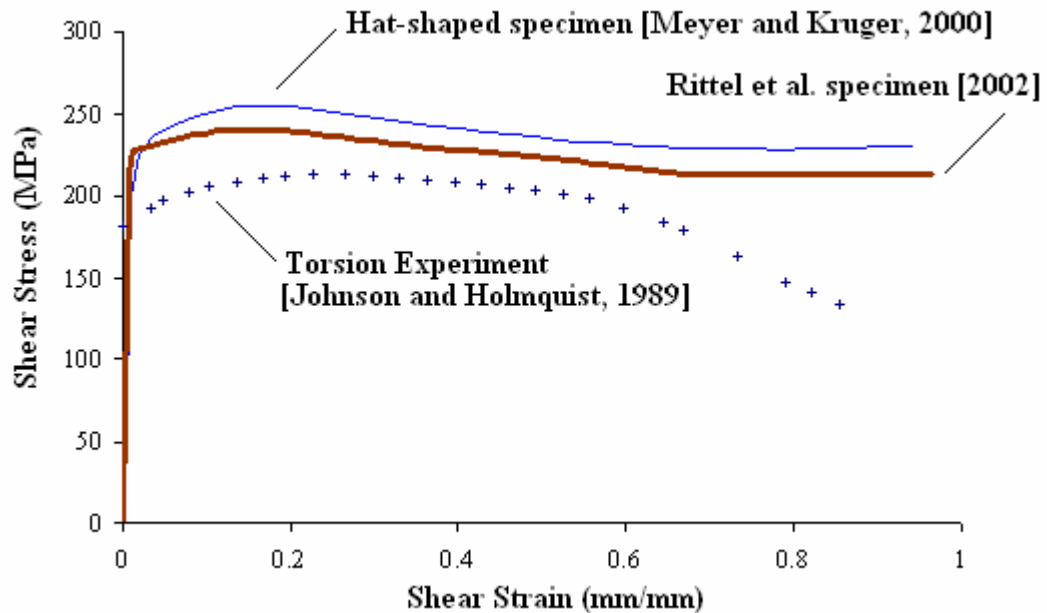


Figure 4.13 Shear stress-strain results ($\sim 2500/s$) recorded in the gage sections of the hat shaped specimen and the shear-compression specimen simulations illustrating the difference in stress states between these two specimens. Dynamic torsion experiments ($232/s$) yield slightly lower stress values.

Dynamic Stress States

Single element simulations were constructed for the three basic stress states—tension, compression, and shear. Each of the simulations was given the same strain history ($\sim 575/s$) and material (Al 6061-T6) to show only the effect of stress state. The calculated stress-strain curves, plotted as Figure 4.14, all differ in magnitude and shape. Compressive stress continued to grow with strain while tension and shear reached some peak stress. Shear strength was the lowest for this material.

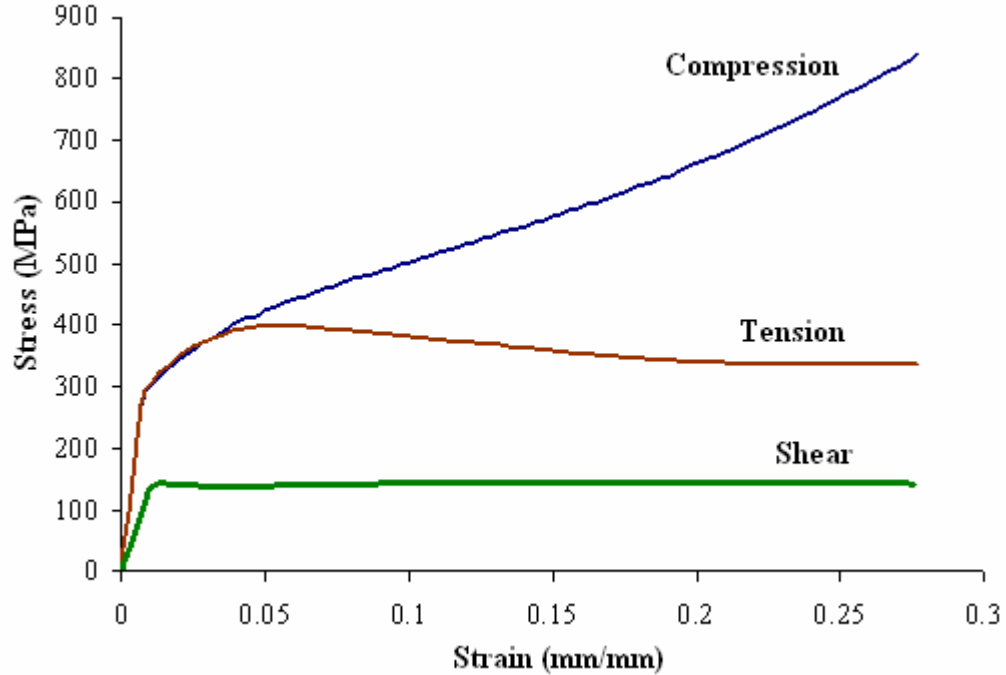


Figure 4.14 Single element simulation stress-strain curves illustrating the material reaction to different stress states. Each case was given the same strain history (~575/s) and material (Al 6061-T6).

Specimen Conclusions

Each of the proposed specimens may be used to produce some practical results, but each one is limited. The m-shaped specimen was shown to overestimate the uniaxial tensile stress. The shear-compression specimen's equivalent stress and strain calculations were shown to be fairly accurate. Equations were presented to estimate the shear stress and strain in the gage section. The hat-shaped specimen was shown to easily yield shear stress results, and an equation was presented to better approximate the shear strain. The experimentalist must know the limitations of these specimens due to the complex stresses produced by their complex geometries.

REFERENCES

- Al-Mousawi, M.M., Reid, S.R., and Deans, W.F. "The Use of the Split Hopkinson Pressure Bar Techniques in High Strain Rate Materials Testing," *Proceedings of the Institution of Mechanical Engineers*, vol. 211, C, 273-292, 1997.
- Bammann, D.J., "Modeling the Temperature and Strain Rate Dependent Large Deformation of Metals," *Applied Mechanics Review*, vol. 43, 5, part 2, S312-S319, 1990.
- Gray III, G.T., "Classic Split-Hopkinson Pressure Bar Testing," *ASM Handbook* (edited by Kuhn, H. and Medlin, D.), vol. 8, 462-476, ASM International, 2000.
- Guo, Y.B., Wen, Q., and Horstemeyer, M.F., "An Internal State Variable Plasticity-Based Approach to Determine Dynamic Loading History Effects on Material Property in Manufacturing Processes," *International Journal of Mechanical Sciences*, vol. 47, 1423-1441, 2005.
- Hartmann, K.-H., Kunze, H.D., and Meyer, L.W., "Metallurgical Effects on Impact Loaded Materials," *Shock Wave and High-Strain-Rate Phenomena in Metals* (edited by Meyers, M. A. and Murr, L. E.), 325-337, Plenum Press, 1981.
- Johnson, G.R. and Holmquist, T.J., "Test Data and Computational Strength and Fracture Model Constants for 23 Materials Subjected to Large Strains, High Strain Rates, and High Temperatures," Los Alamos National Laboratory report, LA-11463-MS, 1-92, 1989.
- Kolsky, H., "An Investigation of the Mechanical Properties of Materials at Very High Rates of Loading," *Proceedings of the Physical Society*, vol. 62, B, 676-700, 1949.
- Livermore Software Technology Corporation, *LS-DYNA Keyword User's Manual*, Livermore, California, 2003.
- Meyer, L.W. and Kruger, L., "Shear Testing with Hat-Shaped Specimen," *ASM Handbook* (edited by Kuhn, H. and Medlin, D.), vol. 8, 451-452, ASM International, 2000.
- Mohr, D. and Gary, G., "M-Shaped Specimen for the High-Strain Rate Tensile Testing Using a Split Hopkinson Pressure Bar Apparatus," *Experimental Mechanics*, accepted for publication, 2007.

Nemat-Nasser, S., "Introduction to High Strain Rate Testing," *ASM Handbook* (edited by Kuhn, H. and Medlin, D.), vol. 8, 427-461, ASM International, 2000.

Rittel, D., Lee, S., and Ravichandran, G., "A Shear-compression Specimen for Large Strain Testing," *Experimental Mechanics*, vol. 42, 1, 58-64, 2002.

CHAPTER 5

CONCLUSIONS

In this study, dynamic material response was determined using an explicit finite element code and a hydrocode. The stress wave behavior and dynamic material response was shown for functionally graded materials, meteorite impacts, and split Hopkinson pressure bar specimens.

Functionally graded materials were modeled as projectiles and as armor. For functionally graded projectiles, the produced shock wave profile was shown to be primarily controlled by the graded materials' densities and secondarily controlled by the graded materials' impedance. Functionally graded armor was found to have the most stopping power when the weaker material was the outermost material and when the grading thickness was largest. For both of the functionally graded cases, projectile and armor, the results can be used to design for dynamic material response.

Meteorite impacts were modeled to show the crust's response to this type of loading. The simulations revealed that these impacts cause more deformation than just a crater; large stress wave magnitudes were found deep in the Earth. Crustal material flow was shown to be highly affected by impact angle and location. This work also showed the need for better boundary conditions in hydrocodes so that more complex geometries may be modeled.

Split Hopkinson pressure bar specimens were modeled to validate their proposed stress and strain calculations. These specimens were designed to produce shear or tensile deformation under compressive loading. The shear or tensile stress-strain results were to be calculated from the recorded end force and displacement. The m-shaped specimen's tensile stress-strain calculations were shown to be fairly accurate when compared to the uniaxial stress-strain response in the gage section. However, both of these stress levels were considerably greater than simple tension simulations and experiments. The shear-compression specimen's equivalent stress-strain calculations were shown to be fairly accurate when compared to the equivalent stress-strain response in the gage section. Equations were proposed to approximate the shear stress and strain in the gage section. These shear equations removed the non-gage compression and were fairly accurate. The hat-shaped specimen's shear stress calculation was shown to be accurate; however, the proposed shear strain calculation was inaccurate. A shear strain equation, which removed the non-gage compression, was proposed and shown to be fairly accurate. The results for all proposed specimens revealed their limitations and the required user knowledge. Stress-strain results must be properly calculated from the recorded force and displacement and then properly interpreted.

APPENDIX A
METEOR IMPACT MATERIALS

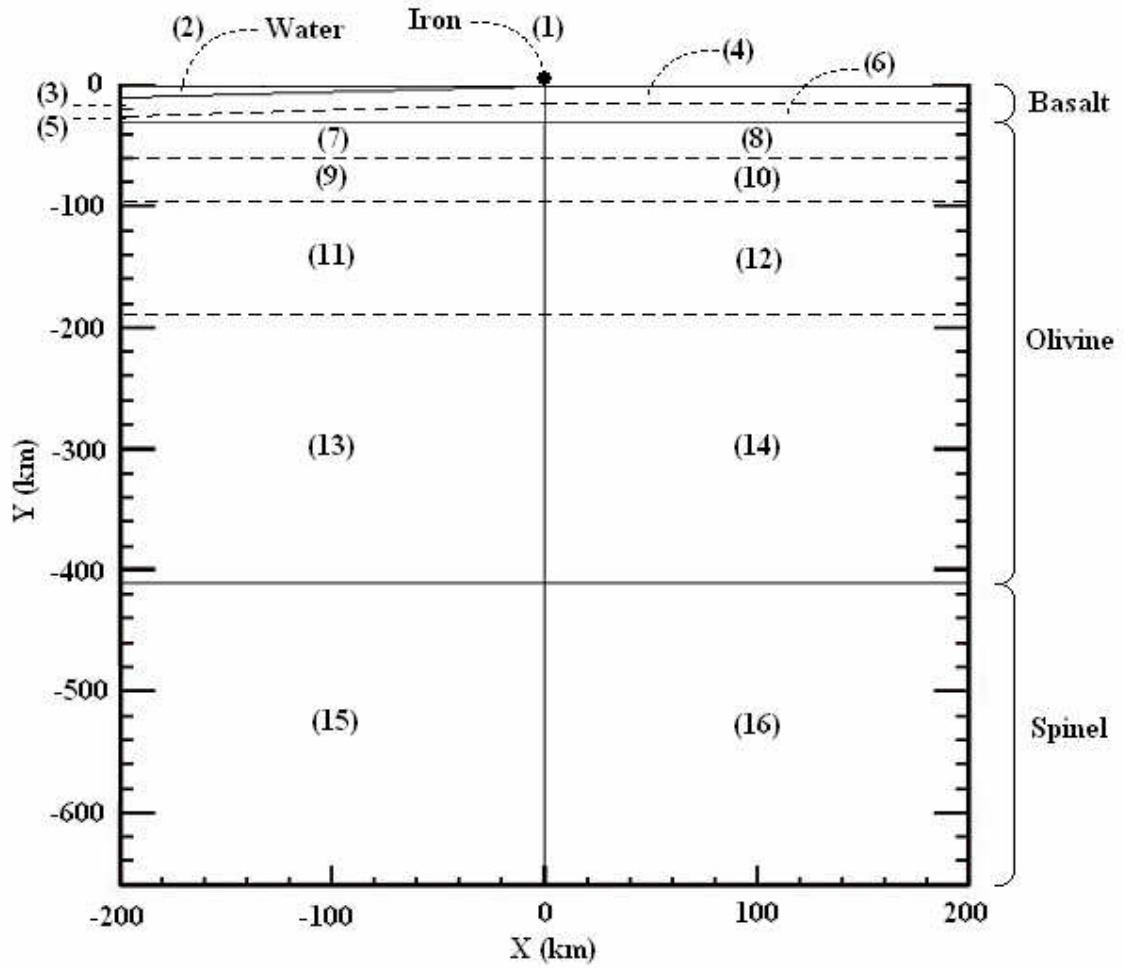


Figure A.1 Material diagram for meteor simulations

Table A.1 Material models for meteor. simulations

| Material (number) | Equation of State | | | | | Plasticity | Fracture | |
|----------------------|-------------------------------------|---|---------------------|-----------------|--|------------|--|-------------------------|
| | Density (grams/cm ³) | Wave Speed | Hugoniot | Grüneisen | Specific Heat Cv (cm ² /s ² /eV) | | | |
| | | Cs (cm/s) | Linear Coeff. SI | Parameter G0 | | | | |
| 1 | | Mie-Grüneisen: Alpha Iron (supplied with CTH) | | | | | Johnson-Cook: Iron (supplied with CTH) | 2.76E+09 (Johnson-Cook) |
| 2 | | Mie-Grüneisen: Water (supplied with CTH) | | | | | | 1 |
| 3 | | Sesame: Basalt (supplied with CTH) | | | | | 1.80E+09 | 1.80E+09 |
| 4 | | Sesame: Basalt (supplied with CTH) | | | | | 1.80E+09 | 1.80E+09 |
| 5 | | Sesame: Basalt (supplied with CTH) | | | | | 1.50E+09 | 1.50E+09 |
| 6 | | Sesame: Basalt (supplied with CTH) | | | | | 1.50E+09 | 1.50E+09 |
| 7 | 3.299 | 560000 | 1.3 | 1.14 | 1.26025E+11 | 2.00E+09 | 2.00E+09 | |
| 8 | 3.322 | 560000 | 1.3 | 1.14 | 1.26025E+11 | 2.00E+09 | 2.00E+09 | |
| 9 | 3.251 | 560000 | 1.3 | 1.1 | 1.34960E+11 | 2.00E+08 | 2.00E+08 | |
| 10 | 3.275 | 560000 | 1.3 | 1.1 | 1.34960E+11 | 2.00E+08 | 2.00E+08 | |
| 11 | 3.200 | 560000 | 1.3 | 1.06 | 1.41111E+11 | 1.00E+08 | 1.00E+08 | |
| 12 | 3.225 | 560000 | 1.3 | 1.06 | 1.41111E+11 | 1.00E+08 | 1.00E+08 | |
| 13 | 3.163 | 560000 | 1.3 | 0.986 | 1.49582E+11 | 5.00E+07 | 5.00E+07 | |
| 14 | 3.189 | 560000 | 1.3 | 0.986 | 1.49582E+11 | 5.00E+07 | 5.00E+07 | |
| 15 | 3.362 | 710000 | 1.13 | 1.107 | 1.68729E+11 | 5.00E+07 | 5.00E+07 | |
| 16 | 3.392 | 710000 | 1.13 | 1.107 | 1.68729E+11 | 5.00E+07 | 5.00E+07 | |

Table A.2 BCJ models for wet and dry olivine at high temperatures

| | Wet Olivine | | | | | | Dry Olivine | | | | | |
|----------------------|-------------|------------|------------|------------|------------|------------|-------------|------------|------------|------------|------------|------------|
| | 700 K | 1100 K | 1500 K | 1900 K | 700 K | 1100 K | 1500 K | 1900 K | 700 K | 1100 K | 1500 K | 1900 K |
| | Density | 3.299 | 3.251 | 3.200 | 3.163 | 3.322 | 3.275 | 3.225 | 3.189 | 3.322 | 3.275 | 3.225 |
| Young's Modulus | 1.815E+12 | 1.684E+12 | 1.555E+12 | 1.473E+12 | 1.815E+12 | 1.684E+12 | 1.555E+12 | 1.473E+12 | 1.815E+12 | 1.684E+12 | 1.555E+12 | 1.473E+12 |
| Poisson's Ratio | 0.252 | 0.255 | 0.260 | 0.263 | 0.252 | 0.255 | 0.260 | 0.263 | 0.252 | 0.255 | 0.260 | 0.263 |
| C1 | 2.20E+08 | 2.20E+08 | 2.20E+08 | 2.20E+08 | 2.20E+08 | 2.20E+08 | 2.20E+08 | 2.20E+08 | 2.20E+08 | 2.20E+08 | 2.20E+08 | 2.20E+08 |
| C2 | 0 | 0 | 0 | 0 | 0 | 0 | 0 | 0 | 0 | 0 | 0 | 0 |
| C3 | 2.00E+08 | 2.00E+08 | 2.00E+08 | 2.00E+08 | 2.00E+08 | 2.00E+08 | 2.00E+08 | 2.00E+08 | 2.00E+08 | 2.00E+08 | 2.00E+08 | 2.00E+08 |
| C4 | 0.051286 | 0.032637 | 0.023933 | 0.018895 | 0.051286 | 0.032637 | 0.023933 | 0.018895 | 0.051286 | 0.032637 | 0.023933 | 0.018895 |
| C5 | 0.00002 | 0.00002 | 0.00002 | 0.00002 | 0.00002 | 0.00002 | 0.00002 | 0.00002 | 0.00002 | 0.00002 | 0.00002 | 0.00002 |
| C6 | 0 | 0 | 0 | 0 | 0 | 0 | 0 | 0 | 0 | 0 | 0 | 0 |
| C7 | 0.001329 | 0.001329 | 0.001329 | 0.001329 | 0.001329 | 0.001329 | 0.001329 | 0.001329 | 0.001329 | 0.001329 | 0.001329 | 0.001329 |
| C8 | 7.31871 | 4.65736 | 3.41540 | 2.69637 | 7.31871 | 4.65736 | 3.41540 | 2.69637 | 7.31871 | 4.65736 | 3.41540 | 2.69637 |
| C9 | 2.935E+11 | 2.935E+11 | 2.935E+11 | 2.935E+11 | 4.512E+11 | 4.512E+11 | 4.512E+11 | 4.512E+11 | 4.512E+11 | 4.512E+11 | 4.512E+11 | 4.512E+11 |
| C10 | 0.00421035 | 0.00661627 | 0.00902219 | 0.01142811 | 0.00421035 | 0.00661627 | 0.00902219 | 0.01142811 | 0.00421035 | 0.00661627 | 0.00902219 | 0.01142811 |
| C11 | 5.000E-14 | 5.000E-14 | 5.000E-14 | 5.000E-14 | 4.521E-12 | 4.521E-12 | 4.521E-12 | 4.521E-12 | 4.521E-12 | 4.521E-12 | 4.521E-12 | 4.521E-12 |
| C12 | 0 | 0 | 0 | 0 | 0 | 0 | 0 | 0 | 0 | 0 | 0 | 0 |
| C13 | 1.520E+13 | 1.520E+13 | 1.520E+13 | 1.520E+13 | 1.550E+17 | 1.550E+17 | 1.550E+17 | 1.550E+17 | 1.550E+17 | 1.550E+17 | 1.550E+17 | 1.550E+17 |
| C14 | 0.72710217 | 0.46270138 | 0.33931435 | 0.26787975 | 1.39404049 | 0.88711667 | 0.65055223 | 0.51359386 | 1.39404049 | 0.88711667 | 0.65055223 | 0.51359386 |
| C15 | 7.039E+11 | 7.039E+11 | 7.039E+11 | 7.039E+11 | 1.720E+12 | 1.720E+12 | 1.720E+12 | 1.720E+12 | 1.720E+12 | 1.720E+12 | 1.720E+12 | 1.720E+12 |
| C16 | 0.00819197 | 0.01287310 | 0.01755423 | 0.02223536 | 0.02186146 | 0.03435372 | 0.04684598 | 0.05933824 | 0.02186146 | 0.03435372 | 0.04684598 | 0.05933824 |
| C17 | 0 | 0 | 0 | 0 | 4.984E-13 | 4.984E-13 | 4.984E-13 | 4.984E-13 | 4.984E-13 | 4.984E-13 | 4.984E-13 | 4.984E-13 |
| C18 | 0 | 0 | 0 | 0 | 0 | 0 | 0 | 0 | 0 | 0 | 0 | 0 |
| C19 | 0 | 0 | 0 | 0 | 0 | 0 | 0 | 0 | 0 | 0 | 0 | 0 |
| C20 | 0 | 0 | 0 | 0 | 0 | 0 | 0 | 0 | 0 | 0 | 0 | 0 |
| Damage Constant | 0 | 0 | 0 | 0 | 0 | 0 | 0 | 0 | 0 | 0 | 0 | 0 |
| Initial Damage | 0 | 0 | 0 | 0 | 0 | 0 | 0 | 0 | 0 | 0 | 0 | 0 |
| Spall Strength | 2.00E+09 | 2.00E+08 | 1.00E+08 | 5.00E+07 | 2.00E+09 | 2.00E+08 | 1.00E+08 | 5.00E+07 | 2.00E+09 | 2.00E+08 | 1.00E+08 | 5.00E+07 |
| Initial Stress A1 | 0 | 0 | 0 | 0 | 0 | 0 | 0 | 0 | 0 | 0 | 0 | 0 |
| Initial Stress A2 | 0 | 0 | 0 | 0 | 0 | 0 | 0 | 0 | 0 | 0 | 0 | 0 |
| Initial Stress A3 | 0 | 0 | 0 | 0 | 0 | 0 | 0 | 0 | 0 | 0 | 0 | 0 |
| Initial Stress A4 | 0 | 0 | 0 | 0 | 0 | 0 | 0 | 0 | 0 | 0 | 0 | 0 |
| Initial Stress A5 | 0 | 0 | 0 | 0 | 0 | 0 | 0 | 0 | 0 | 0 | 0 | 0 |
| Initial Hardening A6 | 0 | 0 | 0 | 0 | 0 | 0 | 0 | 0 | 0 | 0 | 0 | 0 |

APPENDIX B

DYNAMIC SPECIMEN MATERIAL MODEL

Table B.1 Bammann plasticity property values and constants for Al 6061-T6
[Guo et al., 2005]

| Parameter | Value | Units |
|-----------------------------|----------|-----------------------|
| Mass Density | 2.7E-9 | Tonne/mm ³ |
| Modulus of Elasticity | 69000 | MPa |
| Poisson's Ratio | 0.33 | |
| Initial Temperature | 293 | K |
| Heat Generation Coefficient | 0.372024 | Mm ² *K/N |
| C1 | 187.46 | MPa |
| C2 | 1010 | K |
| C3 | 35.97 | MPa |
| C4 | 632.1 | K |
| C5 | 1 | 1/s |
| C6 | 0 | K |
| C7 | 32.344 | 1/MPa |
| C8 | 1433 | K |
| C9 | 988.3 | MPa |
| C10 | 1.331 | K |
| C11 | 5.4E-6 | s/MPa |
| C12 | 252.1 | K |
| C13 | 207000 | 1/MPa |
| C14 | 6394 | K |
| C15 | 85.77 | MPa |
| C16 | 0.06024 | K |
| C17 | 0.00391 | s/MPa |
| C18 | 2468 | K |
| Internal State Variable A1 | 0 | MPa |
| Internal State Variable A2 | 0 | MPa |
| Internal State Variable A3 | 0 | MPa |
| Internal State Variable A4 | 0 | MPa |
| Internal State Variable A5 | 0 | MPa |
| Internal State Variable A6 | 0 | MPa |